

Preferred-Frame and CP -Violation Tests with Polarized Electrons

B. R. Heckel, E. G. Adelberger, C. E. Cramer,*

T. S. Cook, S. Schlamminger, and U. Schmidt†

*Center for Experimental Nuclear Physics and Astrophysics,
Box 354290, University of Washington, Seattle, WA 98195-4290*

(Dated: October 31, 2018)

arXiv:0808.2673v1 [hep-ex] 20 Aug 2008

Abstract

We used a torsion pendulum containing $\approx 10^{23}$ polarized electrons to search new interactions that couple to electron spin. We limit CP-violating interactions between the pendulum's electrons and unpolarized matter in the earth or the sun, test for rotation and boost-dependent preferred-frame effects using the earth's rotation and velocity with respect to the entire cosmos, and search for exotic velocity-dependent potentials between polarized electrons and unpolarized matter in the sun and moon. We find CP-violating parameters $|g_P^e g_S^N|/(\hbar c) < 9.4 \times 10^{-37}$ and $|g_A^e g_V^N|/(\hbar c) < 1.2 \times 10^{-56}$ for $\lambda > 1\text{AU}$. We test for preferred-frame interactions of the form $V = -\boldsymbol{\sigma}^e \cdot \mathbf{A}$, $V = -B\boldsymbol{\sigma}^e \cdot \mathbf{v}/c$, or $V = -\sum \sigma_i^e C_{ij} v_j/c$, where \mathbf{v} is the velocity of the Earth with respect to the CMB restframe and i, j represent the equatorial inertial coordinates X, Y and Z . We constrain all 3 components of \mathbf{A} , obtaining 1σ upper limits $|\mathbf{A}_{X,Y}| \leq 1.5 \times 10^{-22}$ eV and $|\mathbf{A}_Z| \leq 4.4 \times 10^{-21}$ eV that may be compared to the benchmark value $m_e^2/M_{\text{Planck}} = 2 \times 10^{-17}$ eV. Interpreting our constraint on \mathbf{A} in terms of non-commutative geometry, we obtain an upper bound of $(355 l_{\text{GUT}})^2$ on the minimum observable area, where $l_{\text{GUT}} = \hbar c/(10^{16} \text{ GeV})$ is the grand unification length. We find that $|B| \leq 1.2 \times 10^{-19}$ eV. All 9 components of \mathbf{C} are constrained at the 10^{-17} to 10^{-18} eV level. We determine 9 linear combinations of parameters of the Standard Model Extension; rotational-noninvariant and boost-noninvariant terms are limited at roughly the 10^{-31} GeV and 10^{-27} GeV levels, respectively. Finally, we find that the gravitational mass of an electron spinning toward the galactic center differs by less than about 1 part in 10^{21} from an electron spinning in the opposite direction. As a byproduct of this work, the density of polarized electrons in Sm Co_5 was measured to be $(4.19 \pm 0.19) \times 10^{22} \text{ cm}^{-3}$ at a field of 9.6 kG.

PACS numbers: 11.30.Cp, 12.20.Fv

*Current address: Harvard-Smithsonian Center for Astrophysics

†Current address: Physicalisches Institute, Universität Heidelberg

I. INTRODUCTION

This paper describes constraints on possible new spin-coupled interactions using a torsion pendulum containing $\approx 1 \times 10^{23}$ polarized electrons. Several rather different considerations motivated this work. General relativity (the classical theory that forms the standard model of gravity) does not in itself make predictions about the gravitational properties of intrinsic spin—a quantum mechanical effect with no classical analog. Because the classic equivalence-principle and inverse-square-law experiments all used unpolarized test bodies they can shed no light on this issue. In addition, these “fifth force” experiments were completely insensitive to the purely spin-dependent forces arising from the first-order exchange of unnatural parity (0^- , 1^+ , etc) bosons. Lastly, the spin pendulum provided a means to search for a new class of preferred-frame effects that involve intrinsic spin.

We established very tight bounds on long-range CP -violating interactions and on velocity-dependent forces by searching for the effects of unnatural-parity bosons exchanged between the electrons in our pendulum and unpolarized matter in the earth and in the sun. Similarly, we made sensitive searches for preferred-frame effects defined by the entire cosmos. In this case, we checked whether the spins in our pendulum preferred to orient themselves in a direction fixed in inertial space, or if they had a generalized helicity defined by their velocity with respect to the rest-frame of the cosmic microwave background. Finally, we investigated non-commutative space-time geometries and obtained constraints that lie far beyond the reach of any proposed accelerator. In each case, our bounds are interesting because of their high sensitivity. A Letter on the first results from this apparatus has already appeared[1]. This paper, which supercedes Ref. [1], reports additional data and more powerful constraints, provides a complete account of the experimental work, and presents a more extensive discussion of our constraints.

A. Cosmic Preferred Frames

1. General Considerations

It seems natural to us, when testing possible Lorentz-violating preferred-frame scenarios, to let the cosmic microwave background (CMB) define the fundamental inertial frame. We consider, in turn, three types of preferred-frame effects involving spin. First, we consider an

interaction that violates rotational invariance and produces a laboratory potential

$$V = -\boldsymbol{\sigma} \cdot \mathbf{A} , \quad (1)$$

where \mathbf{A} is a preferred direction with respect to the cosmos as a whole. Next, we consider a helicity-generating interaction that violates boost invariance as well, *i.e.* a lab-frame interaction

$$V = -B\boldsymbol{\sigma} \cdot \mathbf{v}/c , \quad (2)$$

where \mathbf{v} is the velocity of the spin with respect to the CMB rest-frame. This velocity has two significant components—the velocity of the earth with respect to the sun ($v_{\odot}/c \sim 10^{-4}$) and the velocity of the sun with respect to the CMB rest frame ($v_{\text{CMB}}/c \sim 10^{-3}$); the small velocity due to the earth’s rotation is neglected.

Finally, following the general ideas of Kostelecký and coworkers[2], we consider a tensor helicity-generating term that produces a laboratory interaction

$$V = -\sum_{i,j} \sigma_i \frac{v_j}{c} C_{ij} . \quad (3)$$

We take Cartesian equatorial coordinates for our inertial frame, where $\hat{\mathbf{Z}}$ points North along the earth’s spin axis, $\hat{\mathbf{X}}$ points from the earth to the sun at the 2000 vernal equinox, and $\hat{\mathbf{Y}} = \hat{\mathbf{Z}} \times \hat{\mathbf{X}}$.

These possible spin-dependent cosmic preferred-frame effects differ from the known CMB preferred-frame effect in two important ways. First, if \mathbf{A} is a time-even polar vector, B a time-even scalar and \mathbf{C} a time-even tensor (untestable assumptions even in principle), then the interactions in Eqs. 1, and either 2 or 3 violate time-reversal and parity, respectively. Second, if such spin-dependent preferred-frame effects exist, they could be observed within an opaque box that shielded out any normal information about the outside world. Although we naively expect that any such preferred-frame effects to be suppressed by the Planck scale and therefore of order $m_e^2/M_{\text{Planck}} \approx 2 \times 10^{-17}$ eV, our results are sufficiently sensitive to probe such tiny effects.

2. The Standard Model Extension effective theory

Kostelecký and coworkers[2] have developed a preferred-frame scenario in which spin-1 and spin-2 fields were spontaneously generated in the early universe and were subsequently

inflated to enormous extents. These fields clearly violate Lorentz symmetry but in a very gentle way. Rotations and boosts of an observer remain Lorentz invariant, but the same operations on a particle (but not the Universe) obviously do not respect the invariance principle. The Lorentz non-invariance invalidates the Pauli-Luders theorem, allowing Kostelecký et al. to construct a field theory with CPT -violating effects (the Standard-Model Extension or SME) that has been widely used to quantify the sensitivity of various CPT and preferred-frame tests involving photons, leptons, mesons and baryons (Ref. [3] has an extensive set of references to this work).

Our \mathbf{A} coefficient is identical to the SME coefficient $\tilde{\mathbf{b}}^e$ which contains contributions from CPT -violating as well as CP -violating terms[4]. The SME has similar terms to our \mathbf{C} coefficients, but they are conventionally expressed in sun-fixed coordinates. To facilitate SME analyses and to compare our results with other work based on SME analyses, we also quote results in which the sun's velocity with respect to the CMB rest frame is ignored.

3. *The Ghost Condensate dynamical theory*

Arkani-Hamed and colleagues have developed a consistent dynamical mechanism for the spontaneous breaking of Lorentz symmetry that, in effect, proposes a pervasive, massless, aether-like fluid consisting of Nambu-Goldstone bosons associated with the broken time-diffeomorphism symmetry[5, 6]. The bosons form a “ghost condensate” because the assumption of translational invariance demands a negative kinetic term in the Lagrangian. They form a condensate because higher-order terms are needed to stabilize the negative kinetic term. This fluid has remarkable properties. Unlike a classical aether, it can be excited. It modifies Newtonian gravity at long ranges and late times in the evolution of the universe. It behaves like a cosmological constant and is capable of accelerating the expansion of the universe, but maximally violates the Equivalence Principle. It defines a preferred frame that converges with the rest frame of the CMB as it reaches equilibrium, and as it evolves to its final state it mimics dark matter. Cosmological tests of gravity limit the diffeomorphism symmetry-breaking scale M to be less than 10 MeV. Interesting physics is possible within this constraint; if M were $\sim 10^{-3}$ eV the condensate could drive the observed acceleration of the universe; if M were ~ 1 eV it would mimic the observed dark matter. Particularly interesting in the present context, a fermion moving with respect to the ghost condensate

experiences an interaction

$$V = \frac{M^2}{F} \boldsymbol{\sigma} \cdot \mathbf{v}/c , \quad (4)$$

where F is a mass scale associated with the coupling of the fermion to the condensate, and \mathbf{v} is the fermion's velocity with respect to the condensate, which we assume to be at rest in the frame where the CMB is essentially isotropic. Equation 4 has the same form as Eq. 2.

B. Non-commutative spacetime geometries

Preferred-frame effects also occur in non-commutative space-time geometries[7, 8] that can arise in D -brane models. In these geometries, the space-time coordinates x_μ do not commute, but instead satisfy

$$[\hat{x}_\mu, \hat{x}_\nu] = i\Theta_{\mu\nu} , \quad (5)$$

where $\Theta_{\mu\nu}$ is a real, antisymmetric tensor that has dimensions of length squared and $|\Theta|$ represents the smallest “observable” patch of area. It is often assumed that $\Theta_{0i} = 0$ to avoid problems with causality. We make the usual additional assumption that $\Theta_{\mu\nu}$ is constant over the space-time region spanned by our experiment, so that it defines a preferred direction $\eta^i = \epsilon^{ijk}\Theta_{jk}$. One consequence of Eq. 5 is that a spinning electron experiences a CP -violating interaction[8, 9]

$$\mathcal{L}_{\text{eff}} = \frac{3}{4}m\Lambda^2 \left(\frac{\alpha}{4\pi\hbar} \right)^2 \Theta^{\mu\nu} \bar{\psi} \sigma_{\mu\nu} \psi , \quad (6)$$

where Λ is a cutoff conventionally taken to be ~ 1 TeV, and α is the fine structure constant. Equation 6 is equivalent to

$$V_e = \boldsymbol{\sigma}_e \cdot \hat{\boldsymbol{\eta}} \left(\frac{\Lambda}{1 \text{ TeV}} \right)^2 3.33 \times 10^{36} \frac{\text{eV}}{\text{m}^2} |\Theta| , \quad (7)$$

which has the same general form as Eq. 1.

C. Forces from exotic boson exchange

The exchange of pseudoscalar particles produces spin-dependent forces that vanish between unpolarized bodies. As a consequence, there are few experimental constraints on such forces. Moody and Wilczek[10] discussed the forces produced by the exchange of low-mass, spin-0 particles and pointed out that particles containing CP -violating $J^\pi = 0^+$ and $J^\pi = 0^-$

admixtures would produce a macroscopic, CP -violating “monopole-dipole” interaction between a polarized electron and an unpolarized atom with mass and charge numbers A and Z

$$V_{eA}(r) = g_P^e g_S^A \frac{\hbar}{8\pi m_\phi c} \boldsymbol{\sigma}_e \cdot \left[\hat{\mathbf{r}} \left(\frac{1}{r\lambda} + \frac{1}{r^2} \right) e^{-r/\lambda} \right], \quad (8)$$

where $m_\phi = \hbar/(\lambda c)$ is the mass of the hypothetical spin-0 particle, g_P and g_S are its pseudoscalar and scalar couplings, and $g_S^A = Z(g_S^e + g_S^p) + (A - Z)g_S^n$. For simplicity, we assume below that $g_S^p = g_S^n = g_S^N$ and $g_S^e = 0$ so that $g_S^A = Ag_S^N$; constraints for other choices of the scalar couplings can be readily obtained by scaling our limits.

Recently Dobrescu and Mocioiu[11] classified the kinds of potentials, constrained only by rotational and translational invariance, that might arise from exchange of low-mass bosons. Our work is sensitive to 3 of their potentials; in addition to a potential equivalent to Eq. 8, we probe the two velocity-dependent potentials

$$V_{eN}(r) = \frac{\boldsymbol{\sigma}_e}{8\pi} \cdot \left[f_\perp \frac{\hbar (\tilde{\mathbf{v}} \times \hat{\mathbf{r}})}{c m_e} \left(\frac{1}{r\lambda} + \frac{1}{r^2} \right) + f_v \frac{\tilde{\mathbf{v}}}{r} \right] e^{-r/\lambda}, \quad (9)$$

where $\tilde{\mathbf{v}}$ is the relative velocity in units of c . Both terms can be generated by one-boson exchange in Lorentz-invariant theories. The parity-conserving f_\perp term can arise from scalar or vector boson exchange, while the parity-violating f_v term can be induced by spin-1 bosons that have both vector and axial couplings to electrons, giving $f_v = 2g_A^e g_V^N$. We constrain the parameters of Eq. 9 by studying the interaction between the polarized electrons in our pendulum and unpolarized nucleons in the sun and moon.

II. APPARATUS

A. Rotating torsion balance

This measurement used a substantially upgraded version of the Eöt-Wash rotating torsion balance that was used for a previous test[12] of the Equivalence Principle. This device, in turn, was an improved version of the instrument described in detail in Ref. [13]. The essential features of this balance are shown in Fig. 1. Briefly, a vacuum vessel containing a torsion pendulum and its associated optical readout system was rotated uniformly about a vertical axis. The pendulum hung in a region of very low magnetic fields and gravity gradients, and the entire instrument was temperature-controlled (stability ± 5 mK). Magnetic fields and

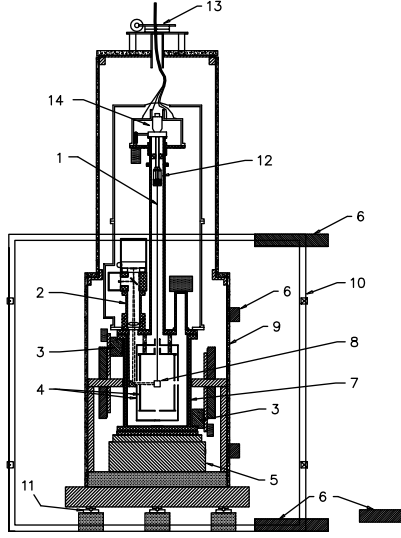


FIG. 1: Scale cross-section of the Eöt-Wash rotating torsion balance; 1: torsion fiber, 2: auto-collimator, 3: Q_{21} gravity-gradient compensator, 4: nested magnetic and electrostatic shields, 5: turntable, 6: Q_{31} gravity-gradient compensator, 7: vacuum vessel, 8: spin pendulum, 9: thermal shield, 10: 3-axis Helmholtz coil system, 11: thermally controlled feet, 12: mode spoiler, 13: co-rotating slip-ring assembly, 14: upper fiber attachment mechanism. Two additional layers of magnetic shielding (not shown for clarity) are immediately inside and outside of the vacuum vessel.

gradients were reduced by a stationary set of Helmholtz coils and 4 layers of co-rotating mu-metal shielding. Gravity gradients were canceled as described in Ref. [13], with a precision that was limited by the fluctuating water content of the ground outside our laboratory.

For this measurement, we made several substantial improvements to the instrument used in Ref. [12]. The turntable was upgraded by a “feet-back” system, described in more detail in Appendix B, that kept its rotation axis vertical to better than 10 nanoradians. The autocollimator system that monitored the pendulum twist was upgraded from that described in Ref. [13] by using the “two bounce” geometry discussed in Ref. [14]. We also improved the resolution of the temperature monitoring system and upgraded the co-rotating magnetic shielding.

The overall performance of the rotating balance is shown in Fig. 2. Except for signals at integer multiples of the turntable frequency caused by reproducible irregularities in the turntable drive system, the noise in the twist signal is close to the thermal value expected from internal losses in the tungsten suspension fiber. Systematic errors associated with the

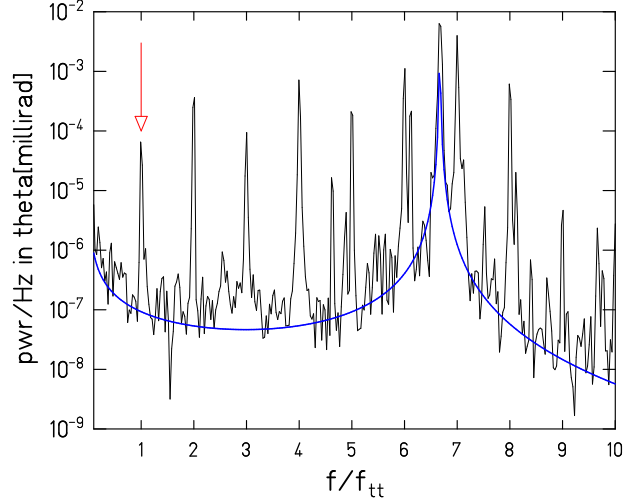


FIG. 2: Spectral power density in the twist signal. The horizontal scale shows the frequency in units of the turntable rotation frequency. The smooth curve shows the expected thermal noise density for this pendulum which had $Q \approx 2000$. At our signal frequency (shown by the arrow) the noise is predominantly thermal. Reproduceable irregularities in the turntable rotation rate produce peaks at integer values of f/f_{tt} . Spurious peaks at odd integer values were suppressed by combining data taken with 2 opposite orientations of the pendulum in the rotating apparatus.

turntable signals were eliminated by combining data taken with different orientations of the pendulum within the rotating apparatus.

B. Spin pendulum

1. Design principles

The heart of our apparatus is a spin pendulum, shown in Fig. 3, that contains a substantial number of polarized electrons while having a negligible external magnetic moment and high gravitational symmetry. The spin pendulum is constructed from 4 octagonal “pucks”. One half of each puck is Alnico 5 (a conventional, relatively “soft” ferromagnet in which the magnetic field is created almost entirely by electron spins) and the other half is grade 22 SmCo₅ (a “hard” rare-earth magnet in which the orbital magnetic moment of the electrons in the Sm³⁺ ion nearly cancels their spin moment[15–17]).

The trapezoidal elements of the pucks were fabricated by electric-discharge machining

and kept in precise alignment by aluminum frames. Thin plates glued to the sides of the Alnico pieces compensated for their lower density, $\rho = 7.37 \text{ g/cm}^3$ versus 8.3 g/cm^3 for Sm Co_5 . After each puck was assembled, we magnetized the Alnico to the same degree as the Sm Co_5 by monitoring the external B fields as appropriate current pulses were sent through coils temporarily wound around the pucks. By stacking 4 such pucks as shown in Fig. 3, we placed the effective center of the spin dipole in the middle of the pendulum, reduced systematic magnetic-flux leakage, averaged out the small density differences between Alnico and Sm Co_5 , and canceled any composition dipole that would have made us sensitive to violation of the weak Equivalence Principle.

The pucks were surrounded by a gold-coated mu-metal shield that supported 4 mirrors equally spaced around the azimuth. The 107 g pendulum was suspended at the end of a 75 cm long tungsten fiber which in turn hung from a mode spoiler that damped the pendulum’s “wobble”, “swing” and “bounce” oscillations but had essentially no effect on the torsional mode. During the course of this experiment 4 different fibers were employed with diameters of either $28 \mu\text{m}$ or $30 \mu\text{m}$. The upper attachment of the suspension fiber could be rotated to place any of the pendulum’s 4 mirrors in the beam of the autocollimator system that monitored the pendulum’s twist.

We measured B_0 , the field inside the pucks, by arranging 11 of the trapezoidal Sm Co_5 elements in straight line, and used an induction coil to determine the field inside the Sm Co_5 . We found $B_0 = 9.6 \pm 0.2 \text{ kG}$ which was consistent with the supplier’s[18] specification of 9.85 kG.

The absolute calibration of the twist to torque conversion was done by observing the pendulum’s response to an abrupt change in the turntable rotation rate as shown in Fig. 4. The pendulum’s free torsional oscillation frequency, $f_0 = 5.379 \text{ mHz}$ for this $30 \mu\text{m}$ diameter fiber, together with its calculated rotational inertia, determined the fiber’s torsional constant $\kappa = 0.185 \text{ dyne-cm/radian}$.

2. *Estimating the spin content*

Polarized neutron elastic scattering studies[15] on Sm Co_5 have shown that the room-temperature magnetic moment of the Sm^{3+} ion is extremely small, $-0.04 \mu_B$ compared to the $-8.97 \mu_B$ moment of the five cobalts (see Appendix A). It is therefore an excellent

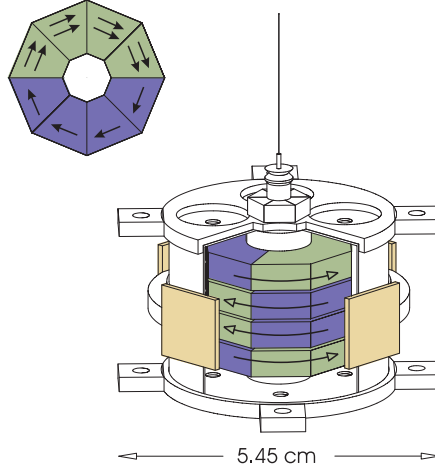


FIG. 3: (color online) Scale drawing of the spin pendulum. The light green and darker blue volumes are Alnico and SmCo_5 , respectively. Upper left: top view of a single “puck”; the spin moment points to the right. Lower right: the assembled pendulum with the magnetic shield shown cut away to reveal the 4 pucks inside. Two of the 4 mirrors (light gold) used to monitor the pendulum twist are prominent. Arrows with filled heads show the relative densities and directions of the electron spins, open-headed arrows show the directions of \mathbf{B} . The 8 tabs on the shield held small screws that we used to tune out the pendulum’s residual q_{21} gravitational moment.

approximation that the magnetization of SmCo_5 is due entirely to the Co. If we make the additional approximation (which we relax below) that the Co and Alnico magnetizations arise entirely from spins, then the net number of polarized spins in our pendulum is simply

$$N_p = \frac{B_0 |R|}{\mu_0 \mu_B} V \eta \quad (10)$$

where B_0 is the magnetic field inside a puck, R is the ratio of Sm to Co spin moments in room-temperature SmCo_5 (a negative quantity because the Sm and Co spins are directed oppositely), $\eta = 0.65$ accounts for the puck’s octagonal shapes and $V = 4.12 \text{ cm}^3$ is the total volume of SmCo_5 . As discussed in Appendix A, we used the Sm ion wavefunctions deduced from elastic neutron scattering[15] on SmCo_5 to predict that at room-temperature the spin contribution to the Sm magnetic moment in SmCo_5 is $\mu_S = +3.56\mu_B$. Using data from this and other rare-earth/cobalt alloys, we estimate that the 5 Co’s in SmCo_5 have $\mu_S = -7.25\mu_B$ and obtain $R = -0.49$.

On the other hand, a Compton scattering experiment on SmCo_5 with circularly polarized synchrotron radiation[17], which directly probes the spin distribution rather than the

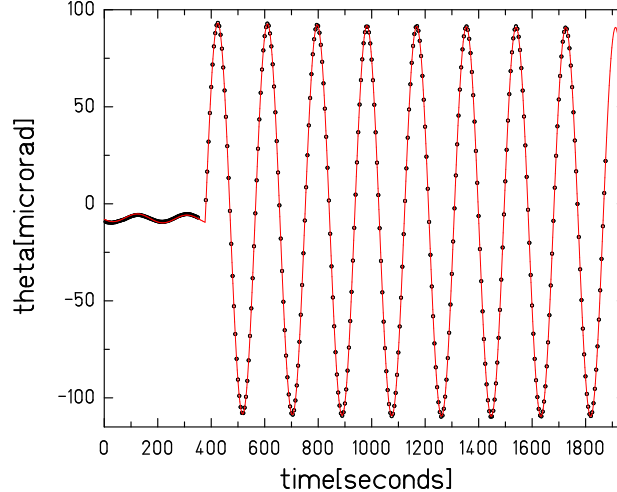


FIG. 4: Dynamical calibration of the torque scale, showing the pendulum twist as a function of time. At $t = 377.7$ s the turntable rotation frequency was abruptly changed from 0.55556 mHz to 0.55611 mHz. The resulting change in the pendulum’s oscillation amplitude and phase calibrated the angular deflection scale and determined the pendulum’s free oscillation frequency f_0 . The smooth curve is the best fit.

magnetic field, gives $R = -0.23$. We assume that R is equally likely to lie anywhere in the interval between -0.49 and -0.23 with a mean value and equivalent Gaussian spread of

$$R = -0.36 \pm 0.075 . \quad (11)$$

which implies $N_p = (0.79 \pm 0.17) \times 10^{23}$.

However, as discussed in Appendix A, experiments have shown that the magnetization of Alnico and of Co in SmCo_5 is not entirely due to spins as we assumed above. Defining f as the fractional contribution of spin to the total magnetic moment, we obtain an improved estimate

$$N_p = \frac{B_0 V \eta}{\mu_0 \mu_B} [f_{\text{Co}}(|R| - 1) + f_{\text{Alnico}}] \quad (12)$$

$$= (0.96 \pm 0.17) \times 10^{23} \quad (13)$$

where $f_{\text{Alnico}} = 0.953 \pm 0.005$ and $f_{\text{Co}} = 0.81 \pm 0.03$ are taken from Eqs. A2 and A4 below.

We show in Sec. VIF below that the Earth’s rotation acting on the pendulum’s angular momentum provided an internal calibration of N_p in very good agreement with the value in Eq. 13.

III. EXPERIMENTAL SIGNATURES

A. General form of the signatures

The potentials of interest (Eqs. 1, 2, 3, 7, 8 and 9) all imply that the pendulum’s energy has the form

$$E = -N_p \boldsymbol{\sigma}_p \cdot \boldsymbol{\beta} , \tag{14}$$

where $\boldsymbol{\sigma}_p$ represents the orientation of the pendulum’s spin, and $\boldsymbol{\beta}$ has a value in the laboratory frame that may depend on time. This potential applies a torque $\boldsymbol{\tau} = N_p \boldsymbol{\sigma}_p \times \boldsymbol{\beta}$ on the pendulum that can be detected by measuring its induced twist. However, only vertical torques, which are resisted by the very soft torsion spring constant, κ , produce a measurable twist; torques in the horizontal plane are resisted by the vastly stronger “gravitational spring” with an effective constant $\kappa_{\text{grav}} = Mgs \approx 2.4 \times 10^6 \kappa$ where M is the pendulum mass and $s = 2.72$ cm is the vertical distance from the pendulum’s center of mass to the fiber attachment point. As a result, the pendulum’s spin is confined to the local horizontal plane and rotates along with the turntable about a vertical axis. Although the pendulum does not exactly follow the turntable angle because external torques on the pendulum twist the suspension fiber by angles $\theta \lesssim 10^{-6}$ radians, to an excellent approximation, the pendulum twist, θ , as a function of turntable angle, ϕ , has the form

$$\begin{aligned} \theta(\phi) &= (\beta_{\perp} N_p / \kappa) \sin(\phi_0 - \phi) \\ &\equiv -(N_p / \kappa) (\beta_N \sin \phi + \beta_E \cos \phi) . \end{aligned} \tag{15}$$

Here β_{\perp} is the projection of $\boldsymbol{\beta}$ on the horizontal plane, ϕ_0 its azimuthal angle, and β_N and β_E are the North and East components of $\boldsymbol{\beta}_{\perp}$. We use the convention that all angles are measured counterclockwise as seen from above, and that $\phi = 0$ points North. The procedure for converting our twist measurements into values for β_N and β_E is discussed in Section V A below.

The scenarios we test in this paper have signatures where $\boldsymbol{\beta}$ is fixed in the laboratory (Eq. 8), and others where $\boldsymbol{\beta}$ is fixed in inertial space (Eqs. 1 and 7) or depends on the orientation and/or velocity of the earth’s motion around the sun (Eqs. 2, 3 and 9). These time-varying signatures were computed using astronomical formulae given by Meeus.[19] We neglected the earth’s radius and the surface velocity associated with its spin in comparison to the astronomical unit and the earth’s orbital velocity, respectively.

B. Lorentz-symmetry violation

We constrained the rotational symmetry violating parameters of Eqs. 1 and 7 by searching for a $\boldsymbol{\beta}$ fixed in inertial space. Even though we are sensitive only to the two horizontal components of $\boldsymbol{\beta}$, the earth's rotation allowed us to probe all three components in the inertial frame,

$$\begin{aligned}\beta_{\text{N}}(t) &= [A_X T_X^{\text{N}}(t) + A_Y T_Y^{\text{N}}(t) + A_Z T_Z^{\text{N}}(t)] \\ &= -(A_X \cos \Omega t + A_Y \sin \Omega t) \sin \Psi + A_Z \cos \Psi \\ \beta_{\text{E}}(t) &= [A_X T_X^{\text{E}}(t) + A_Y T_Y^{\text{E}}(t) + A_Z T_Z^{\text{E}}(t)] \\ &= -A_X \sin \Omega t + A_Y \cos \Omega t .\end{aligned}\tag{16}$$

The $T_{X,Y,Z}^{\text{N,E}}(t)$ coefficients project the equatorial X, Y, Z system onto local N,E horizontal coordinates; $\Psi = 47.658$ deg is the latitude of our laboratory, $\Omega = 2\pi/0.9972696\text{d}$ is the sidereal frequency and t is the local apparent sidereal time.

We measured the boost parameters in Eqs. 2 and 3 using the motion of the earth with respect to the entire cosmos (neglecting the much smaller velocity of our laboratory with respect to the center of the earth). The velocity of the earth with respect to the rest frame of the cosmic microwave background (CMB) is

$$\mathbf{v}_{\oplus} = \mathbf{v}_{\odot} + \mathbf{v}_{\text{CMB}} ,\tag{17}$$

where \mathbf{v}_{\odot} is the velocity of the earth with respect to the sun and \mathbf{v}_{CMB} is the velocity of the sun in the CMB rest frame. In equatorial coordinates

$$\mathbf{v}_{\text{CMB}} = c(-1.190\hat{\mathbf{X}} + 0.253\hat{\mathbf{Y}} - 0.165\hat{\mathbf{Z}})10^{-3}\tag{18}$$

$$\mathbf{v}_{\odot} = v_{\odot}^x \hat{\mathbf{X}} + v_{\odot}^y (\cos \epsilon \hat{\mathbf{Y}} + \sin \epsilon \hat{\mathbf{Z}}) ,\tag{19}$$

where $\epsilon = 23.45$ degrees is the inclination of the ecliptic. The ecliptic coordinate \mathbf{z} is perpendicular to the plane of the earth's orbit, $\mathbf{x} = \mathbf{X}$, and $\mathbf{y} = \mathbf{z} \times \mathbf{x}$ so that

$$\begin{aligned}v_{\odot}^x &= -\dot{R}_{\odot} \cos \lambda_{\odot} + \dot{\lambda}_{\odot} R_{\odot} \sin \lambda_{\odot} \\ v_{\odot}^y &= -\dot{R}_{\odot} \sin \lambda_{\odot} - \dot{\lambda}_{\odot} R_{\odot} \cos \lambda_{\odot}\end{aligned}\tag{20}$$

where $\lambda_{\odot}(t)$, the true longitude of the sun, and $R_{\odot}(t)$, the geocentric distance to the sun, were computed using expressions given by Meeus[19]. Converting \mathbf{v}_{\odot} from ecliptic to equatorial

coordinates, we have

$$\beta_{\text{N,E}}(t) = B \sum_i \frac{v_{\oplus}^i(t)}{c} T_i^{\text{N,E}}(t) , \quad (21)$$

and

$$\beta_{\text{N,E}}(t) = \sum_{i,j} C_{ij} \frac{v_{\oplus}^j(t)}{c} T_i^{\text{N,E}}(t) . \quad (22)$$

Figure 5 shows the signatures of boost-symmetry violating terms with $C_{XX} = 10^{-18}$ eV and with $C_{XZ} = 10^{-17}$ eV. Figure 6 shows how the β_{E} signature varies over the course of a year. The boost-violating signatures, which are modulated at the sidereal, annual and annual times sidereal frequencies, can be distinguished from a violation of rotational-invariance which have only a sidereal modulation. Note that the signatures of A_Z as well as C_{ZX} , C_{ZY} and C_{ZZ} do not have daily modulations and must be extracted from lab-fixed β_{N} 's.

C. Exotic boson-exchange interactions

1. Static potentials

A CP -violating monopole-dipole interaction (Eq. 8) between the spin pendulum and the earth would give time-independent β_{N} and β_{E} values that depend upon the range, λ , of the interaction.

$$\beta_{\text{N,E}} = -\frac{g_{\text{P}}^e g_{\text{P}}^{\text{N}}}{\hbar c} I_{\text{N,E}}(\lambda) , \quad (23)$$

where

$$I_{\text{N,E}}(\lambda) = \hat{\mathbf{e}}_{\text{N,E}} \cdot \int \hat{\mathbf{r}} \left[\left(\frac{1}{r\lambda} + \frac{1}{r^2} \right) e^{-r/\lambda} \right] \frac{K\rho(\mathbf{r})}{u} d^3\mathbf{r} , \quad (24)$$

where \mathbf{r} points from the pendulum to a source mass element with density ρ , $\hat{\mathbf{e}}_{\text{N,E}}$ is a unit vector pointing N or E,

$$K = \frac{\hbar^2}{8\pi m_e} , \quad (25)$$

and u is the atomic mass unit. This integral is, to within a constant factor, identical to that needed to evaluate the Eöt-Wash Equivalence Principle results[13, 20], so we adopted the source integrations of those works. As explained in Refs. [13, 20], the integral can be reliably computed in two regimes: $1 \text{ m} \leq \lambda \leq 10 \text{ km}$ (where information from local topography and boreholes is sufficient, and $\lambda \geq 1000 \text{ km}$ where smooth, layered models of the entire earth are adequate. It is difficult to evaluate the integral in the gap region, and we have not done so. The integrals are displayed in Fig. 7.

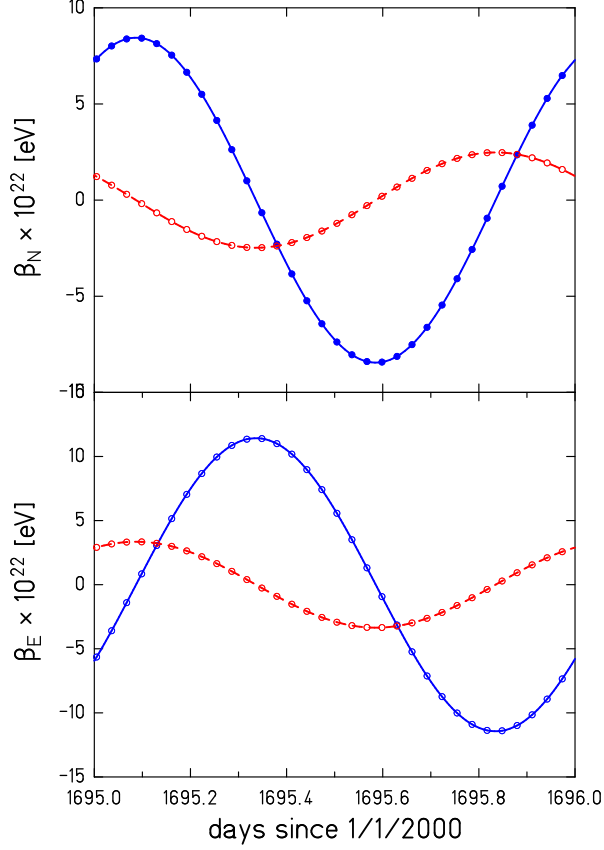


FIG. 5: (color online) Daily signals produced by the Lorentz-boost violating term C_{ij} . The daily signals can be essentially constant (i.e. with a weak annual modulation), modulated at the sidereal frequency, or modulated at both the sidereal and annual frequencies. Solid blue line: $C_{XX} = 10^{-18}$ eV; dashed red line $C_{YY} = 10^{-18}$ eV. The points show the actual times at which data were acquired.

2. Interactions between the spin pendulum and the sun

A CP -violating monopole-dipole interaction (Eq. 8) between the spins in our pendulum and the sun would give modulated β_N and β_E values

$$\begin{aligned}\beta_N(t) &= -(g_P^e g_P^N / \hbar c) I_\odot(\lambda) \cos \alpha_\odot(t) \cos \gamma_\odot(t) / R_\odot^2(t) \\ \beta_E(t) &= -(g_P^e g_P^N / \hbar c) I_\odot(\lambda) \cos \alpha_\odot(t) \sin \gamma_\odot(t) / R_\odot^2(t),\end{aligned}$$

(26)

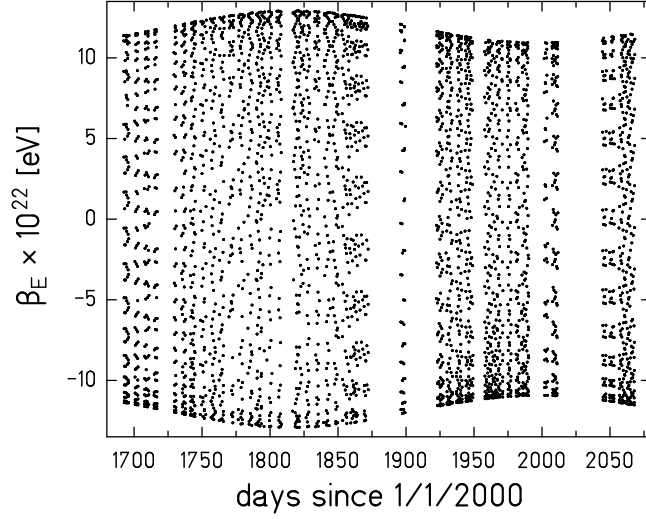


FIG. 6: Expected β_E signal corresponding to $C_{XX} = 10^{-18}$ eV. Each point is placed at the time of one of the cuts in our complete data set. Almost 4000 additional data points extending out to 2825 on the horizontal axis are omitted to keep the figure readable. The annual modulation arises from \mathbf{v}_\odot , the steady component comes from \mathbf{v}_{CMB} .

where α_\odot and γ_\odot are the altitude and azimuth (measured Eastward from North) of the sun. For a uniformly dense sun of mass M_\odot and radius r_\odot , the source integral becomes[21]

$$I_\odot(R_\odot, \lambda) = \frac{K M_\odot}{u} \left[\frac{\xi \cosh \xi - \sinh \xi}{\xi^3/3} \right] \left[\frac{R_\odot}{\lambda} + 1 \right] \exp \left[-\frac{R_\odot}{\lambda} \right], \quad (27)$$

where $\xi = r_\odot/\lambda$.

We searched for the long-range velocity-dependent boson-exchange interactions of Eq. 9 using the earth's velocity around the sun. We needed, in addition to the velocity given in Eq. 20 and $I_\odot(R, \lambda)$, the term $\tilde{\mathbf{v}} \times \hat{\mathbf{r}} = -\dot{\lambda}_\odot R_\odot/c \hat{\mathbf{e}}_z$, and the source integral

$$I_\odot^v(R_\odot, \lambda) = \frac{M_\odot}{8\pi u} \left[\frac{\xi \cosh \xi - \sinh \xi}{\xi^3/3} \right] \exp \left[-\frac{R_\odot}{\lambda} \right]. \quad (28)$$

Then

$$\begin{aligned} \beta_N(t) &= f_\perp I_\odot \dot{\lambda}_\odot (\cos \alpha_z \cos \gamma_z)/(\hbar c^2 R_\odot) \\ &\quad - f_v I_\odot^v (\tilde{v}_x \cos \alpha_x \cos \gamma_x + \tilde{v}_y \cos \alpha_y \cos \gamma_y)/R_\odot \\ \beta_E(t) &= f_\perp I_\odot \dot{\lambda}_\odot (\cos \alpha_z \sin \gamma_z)/(\hbar c^2 R_\odot) \\ &\quad - f_v I_\odot^v (\tilde{v}_x \cos \alpha_x \sin \gamma_x + \tilde{v}_y \cos \alpha_y \sin \gamma_y)/R_\odot \end{aligned} \quad (29)$$

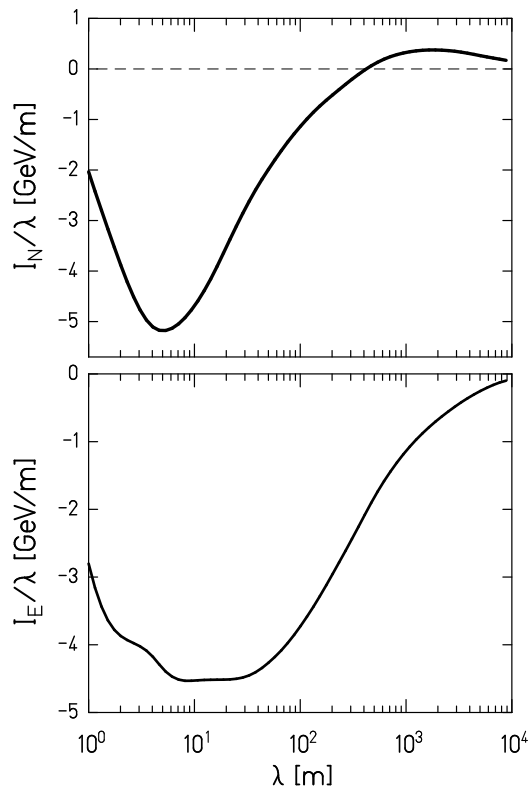


FIG. 7: Earth source integrals defined in Eq. 24. The vertical axis shows $I(\lambda)$ divided by λ . To obtain constraints on $g_{\text{P}}^e g_{\text{P}}^e$ or $g_{\text{P}}^e g_{\text{P}}^p$, rather than on $g_{\text{P}}^e g_{\text{P}}^N$, simply multiply $I(\lambda)$ by $[Z/\mu]_{\oplus} \approx 0.48$.

where $\alpha(t)_{x(y,z)}$ and $\gamma(t)_{x(y,z)}$ are the laboratory altitude and azimuth of the ecliptic unit vectors \hat{x} , \hat{y} and \hat{z} . When evaluating the λ -dependence of the couplings $g_{\text{P}}^e g_{\text{S}}^A$, f_v and f_{\perp} of Eqs. 8 and 9, we approximated the factors R in Eqs. 27-28 by their average value $R = 1$ AU.

3. Interactions between the spin pendulum and the moon

We improved our f_v and f_{\perp} constraints for $\lambda \ll 1$ AU by using the moon's motion about the earth. The moon's coordinates and velocity were evaluated using expressions from Chapter 47 of Meeus[19] to compute generalizations of Eqs. 29 which are more complicated because the moon's motion does not lie in the ecliptic plane and is strongly perturbed by the gradients in the sun's field.

D. Gyro-compass effect

Because the pendulum's magnetic flux was confined entirely within the pucks, the stationary pendulum necessarily contained a net total angular momentum $\mathbf{J} = -\mathbf{S}$, where $S = N_p \hbar/2$ is the pendulum's net spin. The magnetic fields in the two materials,

$$\begin{aligned} B_z(\text{SmCo}_5)/\mu_B &= g_s S_z(\text{SmCo}_5) + g_l L_z(\text{SmCo}_5) \\ B_z(\text{Alnico})/\mu_B &= g_s S_z(\text{Alnico}) + g_l L_z(\text{Alnico}) , \end{aligned} \quad (30)$$

were equal and opposite so that the net magnetic field in the pendulum's z direction vanished. This requires that

$$2\langle S_z^{\text{tot}} \rangle + \langle L_z^{\text{tot}} \rangle = 0 , \quad (31)$$

where we make the excellent approximation that $g_s = 2$. This implies

$$\langle J_z^{\text{tot}} \rangle = -\langle S_z^{\text{tot}} \rangle . \quad (32)$$

To keep \mathbf{J} fixed in the frame of the rotating earth, the fiber has to apply a steady torque, \mathbf{T} , given by

$$\mathbf{T} \cdot \hat{\mathbf{n}} = |\Omega_{\oplus} \times \mathbf{J} \cdot \hat{\mathbf{n}}| , \quad (33)$$

where Ω_{\oplus} is sidereal rotation frequency and $\hat{\mathbf{n}}$ is the local vertical. The pendulum twists until $\kappa\theta = -\mathbf{T} \cdot \hat{\mathbf{n}}$, i.e. \mathbf{J} tries to point toward true North with a torque

$$\mathbf{T} \cdot \hat{\mathbf{n}} = N_p \frac{\hbar \Omega_{\oplus} \cos \Psi}{2} = N_p \times (2.590 \times 10^{-39} \text{ Nm}) , \quad (34)$$

where Ψ is defined in Eq. 16. This is equivalent to a small negative (because $\mathbf{J} = -\mathbf{S}$) value

$$\beta_N^{\text{gyro}} = -1.616 \times 10^{-20} \text{ eV} , \quad (35)$$

which formed a steady, precisely known background in our study of lab-fixed signals, and allowed us to calibrate the spin content of our pendulum.

IV. MEASUREMENTS

The data for this paper were taken in two distinct sets. Runs in set I were taken over a span of 18 months between August 2004 and January 2006. Data were taken with the autocollimator beam reflected by each of the pendulum's 4 mirrors. During this period, along

with acquiring normal spin-pendulum data, we made extensive studies of systematic effects from gravity-gradient and magnetic couplings and from turntable imperfections. Despite considerable effort, that included changing suspension fibers and mode spoilers, we were unable to understand a slowly-varying systematic effect, and as a result our laboratory-fixed constraints were dominated by poorly understood systematics. This work formed the basis of our brief publication[1].

We then decided to tackle the problem of slowly varying systematics by constructing the 93 g “zero-moment” pendulum shown in Fig. 8. This aluminum pendulum had no net spin, was nonmagnetic and had the same moment of inertia as the spin pendulum. It coupled negligibly to gravity gradients because it had cylindrical symmetry and very small q_{20} , q_{30} and q_{40} mass moments. In addition, we modified the fiber attachment to the pendulum so that we could reproducibly rotate the pendulum with respect to its suspension system. As discussed below, this device revealed an unexpected systematic effect associated with the suspension system that could be canceled by combining results taken with opposite orientations of the pendulum with respect to the suspension system.

We added the new rotatable fiber attachment mechanism to the spin pendulum, and set II runs occurred between September 2006 and March 2008. Data were taken with the light beam reflecting from each of the 4 mirrors and for 4 equally spaced angles between the pendulum and the suspension system. The results from set II gave much tighter lab-fixed constraints, and when combined with the set I data improved the sidereal and solar signals published in Ref. [1].

V. DATA ANALYSIS

A. Extracting β_N and β_E from the pendulum twist

Over the course of this experiment the turntable rotation frequency, f , was set at values between $3f_0/29$ and $3f_0/20$, where f_0 is the free-oscillation frequency of the pendulum. We recorded the pendulum twist angle θ as a function of the angle ϕ of the turntable (measured counter clock-wise from North), and converted it to torque, as described in Ref. [13]. Briefly, data were divided into “cuts” each of which contained exactly 2 revolutions of the turntable, lasted no more than 3800 s and typically contained 254 data points. A simple digital filter

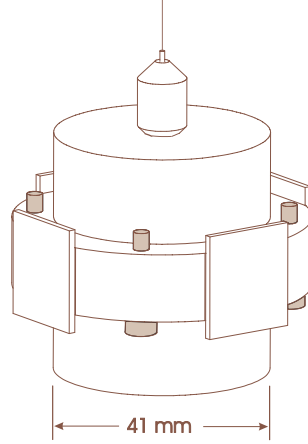


FIG. 8: Scale drawing of the “zero-moment” pendulum. The pendulum body was made from 7075 aluminum. The 4 vertical screws (shaded) were adjusted to trim away the residual q_{21} moments of the pendulum. The “ball-cone” device on top of the pendulum allowed us to rotate the pendulum with respect to the torsion fiber. The entire pendulum, including the mirrors, was coated with gold.

was applied to suppress the free oscillations. The twist data from each cut were then fitted by 2nd-order polynomial “drift” terms (typical drift was $0.5 \mu\text{rad/h}$) and harmonic terms

$$\theta(\phi) = \sum_{n=1}^8 (a_N^n \cos n\phi - a_E^n \sin n\phi) . \quad (36)$$

Our signal was contained in the $n = 1$ coefficients that we denote below as $a_N(\phi_d, \phi_s)$ and $a_E(\phi_d, \phi_s)$, where ϕ_d is the angle of the pendulum (normally its spin dipole) with respect to the turntable and ϕ_s is the angle between the pendulum and its suspension system.

We converted the a_N and a_E signals for each cut into β_N and β_E values using

$$\begin{aligned} \begin{bmatrix} a_N(\phi_d, \phi_s) \\ a_E(\phi_d, \phi_s) \end{bmatrix} &= \begin{bmatrix} \cos \phi_d & \sin \phi_d \\ -\sin \phi_d & \cos \phi_d \end{bmatrix} \begin{bmatrix} \delta_N \\ \delta_E \end{bmatrix} + \begin{bmatrix} \delta_N^t(\phi_s) \\ \delta_E^t(\phi_s) \end{bmatrix} + \\ &\quad \begin{bmatrix} \cos(\phi_d + \phi_s) & \sin(\phi_d + \phi_s) \\ -\sin(\phi_d + \phi_s) & \cos(\phi_d + \phi_s) \end{bmatrix} \begin{bmatrix} \delta_N^s \\ \delta_E^s \end{bmatrix} . \end{aligned} \quad (37)$$

The fit parameters (δ_N, δ_E) are the twists associated with the pendulum itself, so that

$$\beta_{N,E} = \kappa \delta_{N,E} / N_p , \quad (38)$$

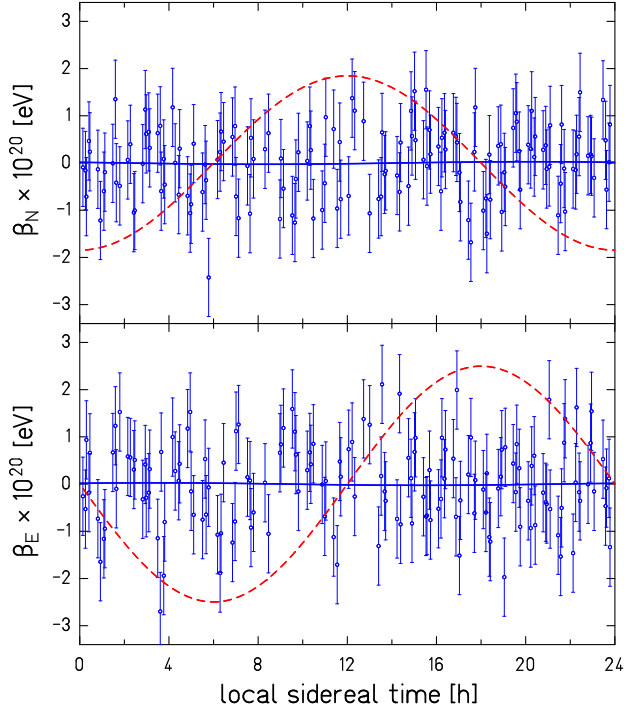


FIG. 9: Data from a set of runs at $\phi_d = 112.5$ deg that spanned a duration of 113 h. The sidereal average of the signals has been set to zero. The dashed curves show the signal from a hypothetical $\mathbf{A} = (2.5 \times 10^{-20} \text{ eV})\hat{\mathbf{x}}$ which gives out-of-phase sine waves in β_N and β_E . The solid curves show the best sidereal fit, which yields $A_x = (-0.20 \pm 0.76) \times 10^{-21} \text{ eV}$ and $A_y = (-0.23 \pm 0.76) \times 10^{-21} \text{ eV}$. (Note that the hypothetical signal in Fig. 2 of Ref. [1] was actually $\mathbf{A} = (2.5 \times 10^{-20} \text{ eV})\hat{\mathbf{x}}$.)

while (δ_N^s, δ_E^s) and (δ_N^t, δ_E^t) are spurious twists associated with the orientations of the suspension system and turntable rotation-rate irregularities, respectively. For data taken with the $30\mu\text{m}$ fiber, $\delta_{N,E} = 1 \text{ nrad}$ corresponds to $\beta_{N,E} = 1.2 \times 10^{-21} \text{ eV}$.

B. Astronomically modulated signals

When analyzing our results for astronomically modulated signals, it was sufficient to ignore the last matrix product term on the right hand side of Eq. 37. We adopted the strategy of Ref. [13] and assumed that β 's modulated at daily, sidereal or yearly periods could be treated as essentially constant during any one cut. This approximation attenuated sidereal signals by at most 0.3% and was neglected. We used linear regression to fit these measured β 's with the expected signatures at the midpoint of each cut. Our input consisted

of 93 data sets (with durations ranging from 1 to 5 days) containing 8471 cuts and spanned a total of 1110 days. We minimized our sensitivity to slow drifts in our signals by zeroing the average values of the twist signals in each data set as well as any steady average value of the predicted signatures. The individual data sets were weighted by the inverse-squares of the spread of the β 's in that set. We constrained \mathbf{A} in Eq. 1 by fitting our data with the two free parameters A_x and A_y given in Eq. 16. Figure 9 shows a typical data set and the fit. The helicity term in Eq. 2 was constrained by fitting Eq. 21 with the single free parameter B . An analysis with 6 free parameters provided the constraints on the 6 modulated boost-symmetry violating \mathbf{C} terms in Eqs. 3 and 22 (only 6 of the 9 C_{ij} 's produce modulated signals because spins pointing along z give a vanishing E signal and a steady N signal). Limits on the boson exchange potentials defined in Eqs. 8 and 9 obtained using the Sun as a source were found by fitting Eqs. 26 and 29 with the 3 free parameters $g_p^e g_S^A$, f_\perp and f_v . Because of the inclination of the earth's rotation axis, these torques have components modulated with a 24 hour period as well as annual modulations. In every case, the resulting fit had $\chi^2/\nu = 0.99$. Because the individual data sets were normalized to $\chi^2/\nu = 1$, a $\chi^2/\nu = 0.99$ for the combined 93 data sets showed that there was no evidence for any anomalous behavior. The sidereal or solar modulation of the signatures eliminated many systematic effects that were fixed in the lab; as a consequence our bounds on A_X and A_Y and on the 6 modulated C terms are tighter than those on A_Z or C_{ZX} , C_{ZY} and C_{ZZ} which are based on the lab-fixed limits discussed below (see Tables VI and VII in Sec. VII).

C. Laboratory-fixed signals

1. Data set I

We analyzed our β_N and β_E data for torques fixed in the lab frame by combining the signals observed for 4 equally-spaced angles, ϕ_d , of the spin dipole within the rotating apparatus. As described in Ref. [1], we observed a scatter that was larger than our statistical uncertainties. This prompted us to study lab-fixed systematic effects with the “zero-moment” pendulum.

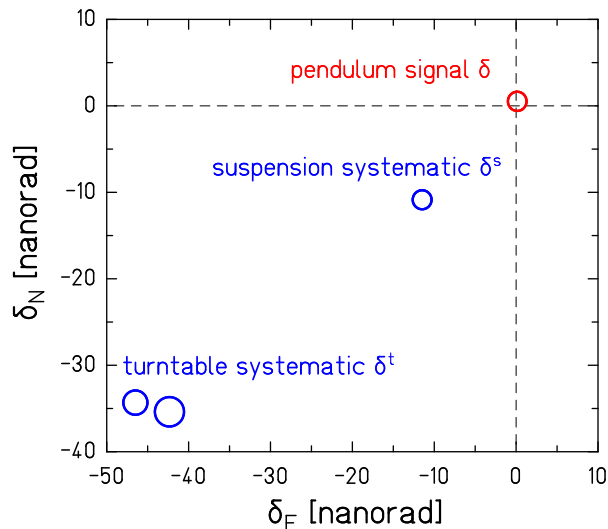


FIG. 10: (color online) Systematic error study using the “zero-moment” pendulum. Data were taken for 4 orthogonal directions of the pendulum with respect to the turntable and for two opposite orientations of the pendulum with respect to its suspension system and fitted with Eq. 37. The ellipses show the values and 1σ uncertainties in the extracted signals associated with the pendulum, the turntable and the suspension system, respectively. Systematic effects associated with the pendulum itself were negligible.

2. Systematic investigations with the zero-moment pendulum

We analyzed data taken on all 4 mirrors and with two opposite orientations of the suspension system with respect to the pendulum using Eq. 37, where the ϕ_d was defined by a fictitious zero mark on the pendulum. The results, shown in Fig. 10, revealed an unexpected systematic effect associated with the pendulum suspension system, along with the known turntable systematic. Figure 10 shows that δ_N^t and δ_E^t changed slightly every time we stopped the turntable and opened the vacuum system to change ϕ_s . Therefore those parameters are shown as functions of ϕ_s in Eq. 37. There was no resolvable systematic effect associated with the pendulum. We therefore base all our lab-fixed constraints on the set II data, which did not suffer from the suspension systematic.

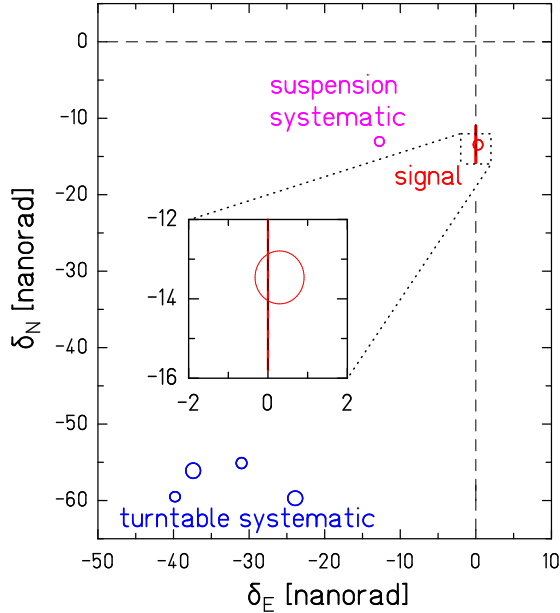


FIG. 11: (color online) Extraction of lab-fixed signals from the October 2006 data, showing the N and E components of the twist signals, obtained using Eq. 37. Ellipses indicate 1σ statistical errors. The turntable systematic changed each time we opened up the vacuum system to change ϕ_{ds} , while the suspension systematic remained constant at a value very close to that seen in the “zero-moment” data plotted in Fig. 10. The red vertical lines shows the expected gyrocompass signal; the length of the line reflects the uncertainty in the R value.

3. Data set II

Spin-pendulum data were acquired with 4 orientations of the pendulum with respect to the rotating apparatus, and for 2 or 4 orthogonal orientations of the suspension system with respect to the pendulum. Three such measurements were taken: Measurement 1 (centered around October 15, 2006), Measurement 2 (centered around June 15, 2007), and Measurement 3 (centered around March 8, 2008). We used Eqs. 37 and 38 to extract from each of these measurement “true” β_N and β_E values that depended only on the orientation of the spin dipole. The extracted values of β_N and β_E for one of these measurements are plotted in Fig. 11. A highly significant signal was observed (see Table V below) that points within 0.2 ± 1.6 degrees of due South; it agrees well with the expected gyro-compass effects discussed in Sec. III D.

VI. SYSTEMATIC ERRORS

The interactions in Eqs. 1–9 all produce 1ω twist signals. Any other mechanism that can produce a 1ω signal is a potential source of systematic error. We present below systematic error analyses for two types of such effects: lab-fixed signals whose amplitude and phase are constant in time and astronomical signals whose amplitude and phase vary as the earth rotates relative to the astronomical source. (Average daily variations of some important environmental parameters are given in Table I). In addition to such “false effects”, we evaluate scale factor uncertainties in N_p , the number of polarized electrons in our pendulum.

TABLE I: Average daily components the systematic effects

effect	daily variation
ambient magnetic field	2.0 ± 0.4 mG
tilt	4.7 ± 2.1 nrad
Q_{22} gravity gradient	$(1.10 \pm 0.27) \times 10^{-3}$ g/cm ³
Q_{21} gravity gradient	$(5.0 \pm 3.4) \times 10^{-4}$ g/cm ³
temperature drift	0.34 ± 0.21 mK
1ω temperature	2.2 ± 1.7 μ K

A. Turntable Rotation Rate

We observed an ≈ 80 nrad 1ω signal that was very reproducible from cycle to cycle and independent of the orientation of the spin pendulum within the rotating apparatus. This arose primarily from a non-constant rotation rate caused by imperfections in the turntable bearings and appeared as a twist signal because we measured the angular position of the “inertial” pendulum relative to the rotating vacuum vessel. Although a servo system locked the output of the turntable’s rotary encoder to a crystal oscillator to produce a nominally constant rotation rate, the finite gain of the servo loop and imperfections in the rotary encoder allowed residual twist signals to appear at the harmonics of the turntable rotation frequency as illustrated in Fig. 2.

We model the true phase, ϕ , of the turntable as

$$\phi = \omega t + \sum_{n=1}^8 \phi_n e^{i\omega_n t}$$

where ω is the nominally constant angular frequency of the turntable, $\omega_n = n\omega$, and ϕ_n is the amplitude of the phase variation due to turntable imperfection. It is easy to show that ϕ_n will produce an angular twist signal, θ_n , at frequency ω_n (ignoring damping) given by

$$\theta_n = \phi_n \frac{\omega_n^2}{\omega_p^2 - \omega_n^2} \quad (39)$$

where ω_p is the free torsional angular frequency of the pendulum.

1. *Astronomical signals*

We searched for time variations, $\Delta\phi_n$, of the turntable imperfections whose amplitudes and phases project onto the time dependence of our astronomical sources by fitting the time sequence of the θ_4 and θ_8 values to the basis functions of each astronomical signal. We chose θ_4 and θ_8 because signals at 4ω and 8ω do not change as the pendulum is rotated to each of its four positions within the vacuum vessel. We found no evidence for a modulation of θ_4 or θ_8 at any of the astronomical frequencies. Furthermore, had there been a coherent modulation, by taking data at all four orientations of the spin pendulum within the vacuum vessel, the 1ω signal from $\Delta\phi_1$ would have been reduced by a factor of 0.22 (more data was taken on mirror 1 than on the other mirrors). Assuming that $\Delta\phi_1 \approx \Delta\phi_4 \approx \Delta\phi_8$ as would be the case for a stiff point on the turntable bearing, and using Eq. 39 with the factor of 0.22, the systematic error from $\Delta\phi_1$ is less than 0.5% of the statistical error for any of the astronomical sources. This error is significantly smaller than the other systematic errors in Tables II and III and was dropped from further consideration.

2. *Lab-fixed signals*

We distinguished lab-fixed sources that couple to the spin dipole of the pendulum from 1ω signals that are independent of the spin dipole by taking data at four equally spaced orientations of the spin dipole within the apparatus. A systematic error can arise if ϕ_1 in Eq. 39 changes as the orientation of the spin dipole is rotated. We searched for such a

TABLE II: Systematic and random errors in the astronomically modulated A , B and C signals evaluated in the CMB rest frame. Corrections were only applied for magnetic effects; the remaining effects were assigned systematic errors equal to the absolute value of the effects plus their 1σ uncertainties. The total systematic errors are quadratic sums of the uncertainty in the magnetic correction and the systematics of the remaining effects. A 2.3% scale-factor uncertainty is not yet included.

signal	systematic error [eV]						random error [eV]
	magnetic	tilt	grav.	gradient	temp. drift	1ω temp.	total
$A_X \times 10^{22}$	$+0.20 \pm 0.07$	± 0.31	± 0.07	± 0.04	± 0.05	± 0.33	± 1.31
$A_Y \times 10^{22}$	-0.10 ± 0.03	± 0.24	± 0.20	± 0.03	± 0.02	± 0.32	± 1.32
$B \times 10^{20}$	-1.40 ± 0.46	± 2.5	± 0.38	± 0.23	± 0.37	± 2.61	± 11.0
$C_{XX} \times 10^{18}$	$+0.95 \pm 0.31$	± 0.43	± 0.17	± 0.08	± 0.05	± 0.57	± 2.16
$C_{XY} \times 10^{18}$	$+2.29 \pm 0.76$	± 0.84	± 0.25	± 0.21	± 0.06	± 1.18	± 4.24
$C_{XZ} \times 10^{18}$	-3.61 ± 1.19	± 2.58	± 0.99	± 0.31	± 0.22	± 3.03	± 10.16
$C_{YX} \times 10^{18}$	-0.73 ± 0.24	± 0.44	± 0.33	± 0.04	± 0.06	± 0.60	± 2.17
$C_{YY} \times 10^{18}$	-1.04 ± 0.34	± 0.76	± 0.67	± 0.15	± 0.07	± 1.08	± 4.25
$C_{YZ} \times 10^{18}$	$+4.02 \pm 1.33$	± 2.46	± 1.60	± 0.21	± 0.32	± 3.24	± 10.23

dependence by comparing the θ_4 and θ_8 signals for the four orientations of the spin dipole and found no variation beyond the statistical error. Assuming that $\Delta\phi_1 \approx \Delta\phi_4 \approx \Delta\phi_8$, Eq. 39 predicts that $\Delta\phi_1$ produces a lab-fixed systematic of 0.11×10^{-22} eV as listed in Table IV.

B. Turntable Tilt

If the rotation axis of the turntable is tilted from local vertical, the upper fiber attachment point flexes as the apparatus rotates, leading to a “tilt-twist” 1ω angular deflection of the pendulum. Imperfections in the mirrors of the system that measures our twist signal produce a related effect as the tilt causes the light spot to move on the mirrors. The tilt of our laboratory floor changes by a few μrad per day which, if not corrected, would produce a spurious 1ω signal that varies by up to 40 nrad per day. The “feedback” control loop

TABLE III: Systematic and random errors in the heliocentrically modulated SME coefficients and one-boson exchange interactions. Corrections were only applied for magnetic effects; the remaining effects were assigned systematic errors equal to the absolute value of effects plus their 1σ uncertainty. The total errors are quadratic sums of the uncertainty in the magnetic corrections and the systematics of the other effects. A 2.3% scale-factor uncertainty is not yet included.

signal	systematic error [eV]					random error [eV]	
	magnetic	tilt	grav.	gradient	temp. drift	1ω temp.	total
$A_X \times 10^{22}$	-0.05 ± 0.02	± 0.30	± 0.06	± 0.05	± 0.05	± 0.31	± 1.44
$A_Y \times 10^{22}$	$+0.08 \pm 0.03$	± 0.21	± 0.17	± 0.03	± 0.02	± 0.27	± 1.44
$C'_{XX} \times 10^{18}$	$+0.94 \pm 0.31$	± 0.44	± 0.18	± 0.08	± 0.05	± 0.58	± 2.16
$C'_{XY} \times 10^{18}$	$+0.73 \pm 0.24$	± 0.64	± 0.23	± 0.12	± 0.06	± 0.73	± 1.98
$C'_{YX} \times 10^{18}$	-0.73 ± 0.24	± 0.44	± 0.33	± 0.04	± 0.06	± 0.60	± 2.17
$C'_{YY} \times 10^{18}$	$+0.70 \pm 0.23$	± 0.56	± 0.08	± 0.16	± 0.11	± 0.64	± 1.99
$f_{\perp}/(\hbar c) \times 10^{32}$	-0.15 ± 0.05	± 0.04	± 0.31	± 0.11	± 0.04	± 0.34	± 2.09
$f_v/(\hbar c) \times 10^{56}$	-1.29 ± 0.43	± 0.68	± 0.14	± 0.07	± 0.12	± 0.83	± 2.32
$g_{\text{P}}^e g_{\text{S}}^N / (\hbar c) \times 10^{37}$	-0.10 ± 0.03	± 1.60	± 0.40	± 0.31	± 0.29	± 1.70	± 8.53

described in Appendix B aligns the rotation axis to within 10 nrad of the local vertical.

We measure the tilt-twist feedthrough (the ratio of the spurious signal to the tilt) by applying known tilts to the apparatus; we find that the feedthrough is typically 3% with an amplitude and phase that depend upon the angular orientation of the pendulum within the apparatus. A conservative upper limit to the component of the tilt-twist feedthrough that mimics a coupling to the spin dipole of the pendulum (*i.e.* that rotates along with the spin dipole) is 4%.

1. Astronomical signals

We extracted any tilt component that mimicked an astronomical signal by fitting the outputs from the rotating tilt sensors to the basis functions of each of the astronomical signals. The largest projection, just over 3 standard deviations, was found for the C_{XY} basis function. We multiplied these tilt projections by the tilt-twist feedthrough, 4%, to

TABLE IV: Error budget for lab-fixed signals. A scale-factor uncertainty equaling 18% of the central value must be folded into the quadratic sum of the random and statistical errors.

date	uncertainty in $\beta \times 10^{22}$ [eV]		
	10/2006	6/2007	3/2008
systematic effect			
tilt	0.52	0.88	0.36
gravity gradient	0.77	0.56	0.65
temp drift	0.14	0.14	0.20
1ω temp	0.14	0.14	0.20
turntable speed	0.11	0.11	0.11
magnetic	1.06	1.06	0.51
total systematic error	1.43	1.50	0.95
random error	7.5	5.6	7.7

determine the systematic error due to tilt. The results, given in Table II, show that control of the tilt-twist feedthrough is the largest source of systematic error for the astronomical signals.

2. Lab-fixed signals

The average tilt of the apparatus was 2.2, 3.7 and 1.5 nrad for lab-fixed Measurements 1, 2 and 3, respectively. The component of the tilt-twist feedthrough that rotated with the orientation of the spin dipole was no more than 2% for these data sets. The lab-fixed systematic error from tilt is then 2% of measured tilt, given in Table IV.

C. Magnetic Coupling

The spin pendulum had a residual magnetic dipole moment of 7×10^{-3} erg/G and was located within four layers of magnetic shielding. When the currents to the Helmholtz coils outside of the apparatus were reversed, a horizontal field of 374 mG was applied to the apparatus which produced a 1ω signal with a typical magnitude of 20 ± 3 nrad ($\beta = 2 \times 10^{-20}$

eV). The spin pendulum was insensitive to reversal of the current in the vertical Helmholtz coil with a feedthrough of less than 2 ± 3 nrad for a 470 mG change in vertical field.

1. *Astronomical signals*

Before taking the data presented in this paper, as well as during the last 20% of the data, a triple-axis fluxgate magnetometer was placed within the Helmholtz coils (but outside of the heat shield) to monitor the stability of the magnetic environment. We were surprised to find an average daily variation of the horizontal magnetic field of 2.0 ± 0.4 mG (see Fig. 12). Because the astronomical signals have a large daily component, the magnetic coupling to daily field variations could lead to systematic errors as large as 56% of the statistical error. To reduce this error, we corrected our data for the coupling to the daily variation of the magnetic field. No other corrections to the astronomical signals were required.

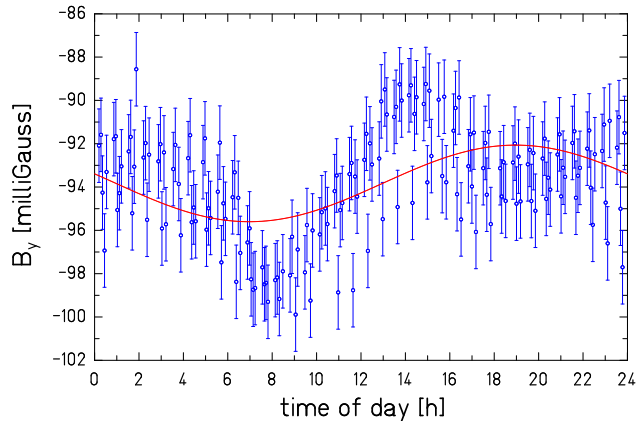


FIG. 12: Daily variation of the ambient magnetic field measured with a flux-gate magnetometer.

The amplitude and phase of the magnetic coupling to the spin pendulum were found by reversing the Helmholtz coil currents, while the fluxgate measurements provided us with the amplitude and phase of the daily variation of the horizontal magnetic field. The calculated magnetic coupling was subtracted from each data cut before fitting the data to the astronomical signal basis functions. We assigned a systematic error for this procedure as follows. For each astronomical signal, we fitted the data with and without the magnetic correction to determine the magnitude of the correction (always less than 56% of the statistical error). There was a 15% uncertainty in the magnetic feedthrough calibration and a 29% uncertainty in the amplitude of the daily magnetic field variation (obtained from the difference between

the measurements before and at the end of the data sequence). We added these uncertainties in quadrature to obtain magnetic systematic errors equal to 33% of the magnetic corrections. Results are listed in Tables II and III.

2. Lab-fixed signals

An applied horizontal field of 374 mG gave a magnetic 1ω signal, S_M , of 22.2 ± 1.4 nrad in Measurements 1 and 2, and 10.8 ± 2.4 nrad in Measurement 3. The Helmholtz coil currents were adjusted to cancel the local field to within 0.5 mG with an uncertainty of 1 mG due to the daily variation of the horizontal field. We compute the magnetic lab-fixed systematic error from $1.5/374 \times S_M$, *i.e.* 0.089 nrad ($\beta = 1.06 \times 10^{-22}$ eV) in Measurements 1 and 2 and 0.043 nrad in Measurement 3.

D. Gravity Gradients

We use a spherical multipole basis[13] to characterize the mass moments, q_{lm} , of the spin pendulum. The coupling of q_{l1} mass moments to Q_{l1} gravity gradient fields produce 1ω angular deflections of the pendulum that have the same dependence upon the orientation of the pendulum as would a coupling to the spin dipole. Although the spin pendulum was designed to have vanishing q_{l1} moments, imperfections produced small residual moments. The only significant gravity gradient coupling for this work was $q_{21}Q_{21}$. This coupling was minimized by using a special gradiometer pendulum with a large q_{21} moment to measure ambient Q_{21} field. We mounted machined Pb/brass masses on a turntable just outside of the vacuum vessel to cancel the local Q_{21} field by a factor of 200. Finally, we temporarily rotated the Pb/brass masses to double the gradient, measured the residual q_{21} moment of the pendulum, and adjusted tuning screws on the pendulum (see Fig. 3) to minimize the residual q_{21} mass moment. By canceling the Q_{21} field and minimizing the q_{21} moment of the pendulum, the $q_{21}Q_{21}$ coupling was reduced to tolerable levels.

1. *Astronomical signals*

We were concerned that daily variations of the local Q_{21} field might couple to the residual q_{21} moment of the pendulum to produce a daily modulated 1ω signal that would project onto the astronomical signal basis functions. The Q_{22} field from local sources is typically larger than the Q_{21} field (because Q_{22} is maximum at a polar angle of 90° where Q_{21} vanishes) and falls off with distance with the same radial dependence as the Q_{21} field. The pendulum had a residual q_{22} moment (uncompensated) that was 7 times larger than the residual q_{21} moment. We used the $q_{22}Q_{22}$ coupling to monitor the time variation of the Q_{22} field which for local sources will be correlated with changes in the Q_{21} field. The $q_{22}Q_{22}$ coupling produces a 2ω signal. We fitted the time sequence of the measured 2ω signals to the astronomical basis functions to determine the projection of any Q_{22} variations onto those functions. We then ran a correlation analysis between the 1ω and 2ω signals over the entire data set to extract the linear slope between the 1ω and 2ω signals. That slope was found to be less than 3%. The gravity gradient systematic error in Table II is the projection of the 2ω signal onto the basis functions times 0.03.

An independent analysis of the daily variation of the Q_{21} field was made using 8 day-long data runs with the gradiometer pendulum. The gradiometer pendulum had a q_{21} moment 90 times larger than the residual moment of the spin pendulum. No evidence for a daily variation in the Q_{21} field was found with an uncertainty 4 times larger than that obtained from the $q_{22}Q_{22}$ analysis.

2. *Lab-fixed signals*

When the Pb/brass Q_{21} compensation masses were rotated to add to the local Q_{21} gradient, a change in 1ω signal of 70 nrad typically was measured. This coupling would change each time the ball-cone attachment on the spin pendulum was rotated because of small changes in the tilt of the pendulum relative to the ball-cone. The residual 1ω signal when the Pb/brass compensators canceled the local gradient was therefore less than 0.2 nrad, typically 20% of the statistical error for each ball-cone configuration. Because we knew the amplitude and phase of the total Q_{21} field and the amplitude and phase of the residual q_{21} moment for each ball-cone configuration, we corrected the raw data for the residual $q_{21}Q_{21}$

coupling. This was the only correction applied to the lab-fixed signals and never exceeded 30% of the statistical error for any configuration. The largest uncertainty in this procedure was the assumption that the total Q_{21} field at the pendulum did not change appreciably with time. We assign a systematic error to this procedure by taking the difference between the lab-fixed signals with and without the $q_{21}Q_{21}$ correction applied, and multiplying this difference by 50% to account for possible changes in the Q_{21} field.

E. Thermal Effects

The equilibrium twist angle of the spin pendulum is a strong function of temperature. Because these and other thermal effects are difficult to model, we took special care to stabilize and monitor the thermal environment of the apparatus. Four temperature sensors were mounted on the rotating apparatus, four others were attached to stationary components of the apparatus, and two sensors monitored the lab air temperature. Constant-temperature water from one Neslab RTE-221 unit flowed through copper pipes soldered to copper heat shields that surround the apparatus, and water from a second unit flowed through radiators with fans to hold constant the temperature of the room that houses the apparatus. The resulting thermal environment for the pendulum is constant to within a few mK per day.

We consider two thermal effects. The first is the direct effect of a temperature change on the 1ω signal of the pendulum. We measured that a 1 K change in temperature of the apparatus caused a 9 ± 4 nrad change in the 1ω signal ($\beta = 1.7 \times 10^{-20}$ eV/K averaged over the sensors). Second, the temperature sensors on the rotating apparatus show small variations (≈ 0.1 mK) at the turntable rotation frequency. Part of this signal may be due to friction in the turntable bearings which, if changing in time, could lead to changes in the 1ω signal of the pendulum.

1. Astronomical signals

We determined the direct temperature effect by fitting the measured mean temperatures of the sensors on the apparatus to the astronomical basis functions. We then multiplied these by the measured feedthrough, 1.7×10^{-20} eV/K, to obtain the systematic errors given as “temp. drift” in Table II. Similarly, we found the 1ω temperature effect by fitting

the 1ω signals of the rotating temperature sensors to the astronomical basis functions and multiplied by the feedthrough. We determined the feedthrough by performing a correlation analysis between the 1ω signals on the rotating temperature sensors and the 1ω signal of the pendulum. The feedthrough was found to be $\leq 160 \times 10^{-20}$ eV/K. The systematic error is given as “ 1ω temp.” in Table II.

2. Lab-fixed signals

The standard deviation of the average temperature of the sensors on the apparatus for the lab-fixed data runs was 2.8 mK. Because there was no correlation between the average temperature and the orientation of the spin pendulum within the apparatus, the direct temperature feedthrough created a random variation of the 1ω pendulum signal. The systematic error for the temperature drift effect, given in Table IV is $2.8 \text{ mK} \times 1.7 \times 10^{-20} \text{ eV/K} / \sqrt{N-1}$ where N is the number of data runs. In measurements 1 and 2, $N = 16$, while measurement 3 had $N = 8$. The standard deviation of 1ω signals on the rotating temperature sensors for the lab fixed data runs was 28 μK . Again, these signals were not correlated with the orientation of the spin pendulum and would produce a random error. We used the same feedthrough for the bearing friction temperature effect as above for the astronomical signals to assign a systematic error for the 1ω temperature feedthrough of $28 \mu\text{K} \times 160 \times 10^{-20} \text{ eV/K} / \sqrt{N-1}$ for the lab-fixed measurements.

F. Spin content of the pendulum

The uncertainty in the pendulum’s spin content adds a scale-factor uncertainty to all our constraints.

1. Lab-fixed signals

Our constraints on A_Z , C_{ZX} , C_{ZY} , C_{ZZ} and the CP -violating interaction of Eq. 8 with $\lambda \ll 1$ A.U. are derived from laboratory-fixed signals. In this case we adopt the spin content and its 18% uncertainty given in Eq. 13.

2. Astronomical signals

Our constraints on these signals are based on effects occurring at sidereal or solar frequencies, and steady lab-fixed β 's were ignored in the analysis. This allowed us to evaluate the constraints using a more precise experimental value for the spin content based on the fact that it is extremely unlikely that new fundamental physics could have produced the lab-fixed signal in Table V. This would require either a preferred-frame \mathbf{A} that happened to point exactly opposite to the Earth's spin axis (this has a probability $\Delta\Omega/(4\pi) \approx [\delta\beta_E \cos\Psi/(2\beta_N)]^2 = 7 \times 10^{-5}$) or a CP -violating interaction of Eq. 8 with $R_\oplus \leq \lambda \leq 3 \times 10^6$ km. If we neglect these unlikely possibilities, our measured torque $\kappa\delta_N = -(0.2537 \pm 0.0057)$ fN m provides, via Eq. 34, an absolute calibration of the spin content of our pendulum,

$$N_p^{\text{exp}} = (9.80 \pm 0.22) \times 10^{22}, \quad (40)$$

which gives a 2.3% scale-factor uncertainty for the astronomically signals. This was always negligible in comparison to the statistical error.

VII. RESULTS

In this section all constraints given in numerical form are 1σ and include both random and systematic errors. Constraints presented in graphical form are at the 95% confidence level.

A. Preferred-frame constraints

1. Phenomenological cosmic preferred frames

To constrain the parameters \mathbf{A} and \mathbf{C} we require results from lab-fixed as well as astronomically modulated signals because the A_Z , C_{ZX} , C_{ZY} and C_{ZZ} signatures have no sidereal modulation. The lab fixed results are displayed in Table V; the combined result of the three measurements is

$$\begin{aligned} \hat{\beta}_N &= (-0.03 \pm 0.28) \times 10^{-20} \text{ eV} \\ \beta_E &= (0.00 \pm 0.04) \times 10^{-20} \text{ eV}, \end{aligned} \quad (41)$$

where $\hat{\beta}_N \equiv \beta_N - \beta_N^{\text{gyro}}$, and the overall scale factor error from the uncertainty in N_p is now included. The results in Table V allow us to extract values for either A_Z , or else for C_{ZX} , C_{ZY} and C_{ZZ} . The result in Eq. 41 implies that

$$\begin{aligned} A_Z &= \hat{\beta}_N / \cos \Psi \\ &= (-0.4 \pm 4.4) \times 10^{-21} \text{ eV} . \end{aligned} \quad (42)$$

On the other hand, to constrain the boost terms we must invert the equations

$$\begin{aligned} \tilde{v}_X(t_1) C_{ZX} + \tilde{v}_Y(t_1) \tilde{C}_{ZY} + \tilde{v}_Z(t_1) \tilde{C}_{ZZ} &= \hat{\beta}_N(t_1) / \cos \Psi \\ \tilde{v}_X(t_2) C_{ZX} + \tilde{v}_Y(t_2) \tilde{C}_{ZY} + \tilde{v}_Z(t_2) \tilde{C}_{ZZ} &= \hat{\beta}_N(t_2) / \cos \Psi \\ \tilde{v}_X(t_3) C_{ZX} + \tilde{v}_Y(t_3) \tilde{C}_{ZY} + \tilde{v}_Z(t_3) \tilde{C}_{ZZ} &= \hat{\beta}_N(t_3) / \cos \Psi . \end{aligned}$$

where \tilde{v} is the laboratory velocity in units of c and t_i refers to the mean time of a lab-fixed measurement given in Table V. We obtain

$$\begin{aligned} C_{ZX} &= (-4.9 \pm 8.8 \pm 0.9) \times 10^{-18} \text{ eV} \\ C_{ZY} &= (-9.6 \pm 18.9 \pm 8.8) \times 10^{-18} \text{ eV} \\ C_{ZZ} &= (+24.8 \pm 38.6 \pm 20.9) \times 10^{-18} \text{ eV} , \end{aligned} \quad (43)$$

where the second error reflects the scale factor uncertainty.

Our complete constraint on the electron's Lorentz-symmetry violating rotation parameter \mathbf{A} is displayed in Table VI; it is roughly two orders of magnitude more restrictive than previous work by Hou *et al.*[22], and substantially below the benchmark value $m_e^2/M_{\text{Planck}} = 2 \times 10^{-17} \text{ eV}$.

Our 1σ constraint on the electron's helicity-generating parameter B is

$$B = (+0.50 \pm 1.13) \times 10^{-19} \text{ eV} . \quad (44)$$

Table VII displays our limits on the electron's generalized helicity tensor \mathbf{C} . We are not aware of any comparable measurements of either B or C .

2. Standard Model Extension

The minimal Standard Model Extension or SME incorporates the possibility of Lorentz and CPT violation by invoking pervasive, feeble, static spin 1 and spin 2 fields that are

TABLE V: Three separate measurements of lab-fixed signals. Units of torque, $\kappa\delta$ and $\beta = \kappa\delta/N_p$ are 10^{-16} N m and 10^{-20} eV, respectively. Dates refer to the mean time of the measurements. Errors in β include the systematic and random errors given in Table IV but not the scale-factor uncertainty.

signal	15/10/06 value	15/6/07 value	8/3/08 value
$\kappa\delta_N$	-2.49 ± 0.11	-2.57 ± 0.08	-2.52 ± 0.12
β_N	-1.62 ± 0.07	-1.67 ± 0.05	-1.64 ± 0.08
β^{gyro}	-1.62	-1.62	-1.62
$\beta_N - \beta^{\text{gyro}}$	$+0.00 \pm 0.07$	-0.05 ± 0.05	-0.02 ± 0.08
$\kappa\delta_E$	$+0.04 \pm 0.11$	-0.06 ± 0.08	$+0.08 \pm 0.12$
β_E	$+0.03 \pm 0.07$	-0.04 ± 0.05	$+0.05 \pm 0.08$

TABLE VI: 1σ constraints from our work and from Hou et al.[22] on the Lorentz-violating rotation parameters defined in Eq. 1. Units are 10^{-22} eV. The errors in A_Z are larger than those in A_X and A_Y because of the greater systematic uncertainty in lab-fixed signals. It is assumed that C terms can be neglected.

parameter	this work	Hou et al.[22]
A_X	-0.67 ± 1.31	-108 ± 112
A_Y	-0.18 ± 1.32	-5 ± 156
A_Z	-4 ± 44	107 ± 2610

defined in the heliocentric frame (for electrons in Minkowski spacetime 44 free parameters are involved).

We follow conventional experimental practice[22–25] and first ignore possible violations of boost symmetry. Then our constraints on \mathbf{A} (Table VI) translate directly to constraints on the SME parameters $\tilde{\mathbf{b}}^e$. Table VIII compares the electron’s $\tilde{\mathbf{b}}$ parameters to the corresponding proton and neutron parameters determined from hydrogen maser[23, 24] and dual $^{129}\text{Xe}/^3\text{He}$ maser measurements[25]. The neutron and electron parameters have comparable upper limits. The hydrogen maser results have an uncertainty 10^4 times greater so, in effect,

TABLE VII: 1σ constraints on the C parameters of Eq. 3. The last three rows in this table are inferred from lab-fixed measurements. Units are 10^{-18} eV and the scale factor uncertainty is included.

parameter	value	parameter	value
C_{XX}	$+0.96 \pm 2.16$	C_{YX}	-3.74 ± 2.17
C_{XY}	$+1.84 \pm 4.24$	C_{YY}	-7.76 ± 4.25
C_{XZ}	-3.92 ± 10.16	C_{YZ}	$+16.17 \pm 10.23$
C_{ZX}	-4.92 ± 8.86		
C_{ZY}	-9.6 ± 20.9		
C_{ZZ}	$+24.8 \pm 43.9$		

they place a substantially weaker limit on $\tilde{\mathbf{b}}$ of the proton.

TABLE VIII: 1σ constraints on the Lorentz-violating rotation parameters for electrons, protons and neutrons. The SME boost terms are assumed to be negligible. Units are 10^{-22} eV. Proton and neutron results are taken from Refs. [23],[24] and Ref. [25], respectively.

parameter	electron	proton	neutron
\tilde{b}_X	-0.67 ± 1.31	$\leq 2 \times 10^4$	0.22 ± 0.79
\tilde{b}_Y	-0.18 ± 1.32	$\leq 2 \times 10^4$	0.80 ± 0.95
\tilde{b}_Z	-4 ± 44		

We constrained boost terms in the SME by reevaluating our limits after setting the velocity of the sun to zero. The resulting boost-dependent coefficients are denoted by primes. The sidereally modulated data were fitted with 6 free parameters, A_X , A_Y , C'_{XX} , C'_{XY} , C'_{YX} and C'_{YY} . In addition, we used the lab-fixed results in Table V to constrain A_Z , C'_{ZX} and

$$\bar{C}'_{ZY} \equiv C'_{ZY} + \tan \epsilon C'_{ZZ} . \quad (45)$$

The A and C' coefficients determine[26] the following combinations of SME parameters

$$A_X = \tilde{b}_X^e \quad A_Y = \tilde{b}_Y^e$$

$$\begin{aligned}
C'_{XX} &= [\tilde{b}_T + \tilde{d}_- - 2\tilde{g}_c - 3\tilde{g}_T + 4\tilde{d}_+ - \tilde{d}_Q]/2 \\
C'_{XY} &= (\tilde{d}_{XY} - \tilde{H}_{ZT}) + \tan \epsilon \tilde{H}_{YT} \\
C'_{YX} &= \tilde{H}_{ZT} \\
C'_{YY} &= [2\tilde{g}_c - \tilde{g}_T - \tilde{b}_T + 4\tilde{d}_+ - \tilde{d}_- - \tilde{d}_Q]/2 + \\
&\quad \tan \epsilon [\tilde{d}_{YZ} - \tilde{H}_{XT}] \\
C'_{ZX} &= \tilde{H}_{YT} - \tilde{d}_{ZX} & C'_{ZY} &= -\tilde{H}_{XT} \\
C'_{ZZ} &= [\tilde{g}_T - 2\tilde{d}_+ + \tilde{d}_Q] .
\end{aligned} \tag{46}$$

Our values for these parameters are listed in Table IX.

TABLE IX: 1σ constraints on electron SME parameters from this experiment. Scale factor errors are included. The A coefficients listed here differ from those in Table VI because here we included additional boost terms whose functional forms are not fully orthogonal to those of the A coefficients.

parameter	electron value (GeV)
A_X	$(-0.9 \pm 1.4) \times 10^{-31}$
A_Y	$(+0.9 \pm 1.4) \times 10^{-31}$
A_Z	$(-0.3 \pm 4.4) \times 10^{-30}$
C'_{XX}	$(+0.9 \pm 2.2) \times 10^{-27}$
C'_{XY}	$(+0.1 \pm 1.8) \times 10^{-27}$
C'_{YX}	$(-4.1 \pm 2.4) \times 10^{-27}$
C'_{YY}	$(-0.8 \pm 2.0) \times 10^{-27}$
C'_{ZX}	$(-4.9 \pm 8.9) \times 10^{-27}$
\bar{C}'_{ZY}	$(+1.1 \pm 9.2) \times 10^{-27}$

3. Ghost condensate gravity

The result in Eq. 44 provides a limit on $-M^2/F$ (see Eq. 4) of

$$\frac{M^2}{F} = (-0.50 \pm 1.10) \times 10^{-19} \text{ eV} , \tag{47}$$

which improves on the value given in Ref. [6] by three orders of magnitude. The corresponding 95% confidence constraint on the “ghost condensate parameter” M/F is shown as a function of M in Fig. 13. A condensate-mediated spin-spin interaction with a strength comparable to gravity would have the ghost condensate parameter $M/F \sim 10^{-16}$ [6].

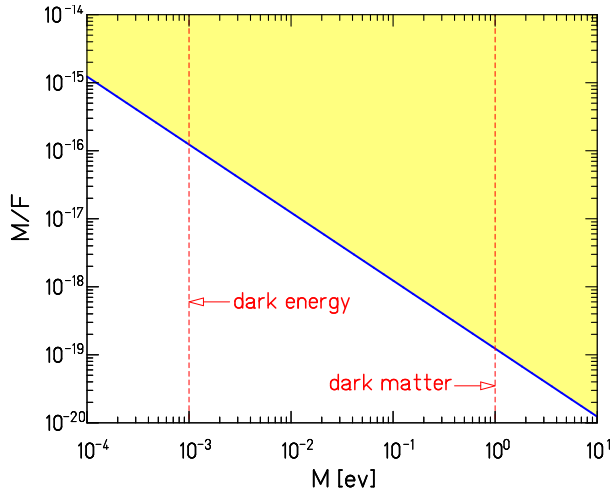


FIG. 13: (color online) Upper limits on the “ghost condensate” parameter M/F as a function of M . The shaded area is excluded at 95% confidence. The vertical dashed lines show values of M having particular cosmological significance.

4. Non-commutative geometry

Inserting the constraint on $|\mathbf{A}|$ from Table VI into Eq. 7, we obtain an 1σ upper limit on $|\Theta|$, the minimum observable patch of area,

$$|\Theta_{XZ}| \text{ or } |\Theta_{YZ}| \leq 4.9 \times 10^{-59} \text{ m}^2 [1 \text{ TeV}/\Lambda]^2 \quad (48)$$

$$|\Theta_{XY}| \leq 1.5 \times 10^{-57} \text{ m}^2 [1 \text{ TeV}/\Lambda]^2 \quad (49)$$

which, assuming $\Lambda = 1 \text{ TeV}$, corresponds to energy scales of $2.8 \times 10^{13} \text{ GeV}$ for Θ_{XZ} or Θ_{YZ} and $5.0 \times 10^{12} \text{ GeV}$ for Θ_{XY} .

5. Axial torsion

Many theorists (see Refs. [30] for a recent review) have speculated that the Riemann geometry of general relativity should be replaced by the more general Riemann-Cartan

geometry that contains an additional non-symmetric field called torsion. Torsion does not directly couple to unpolarized matter and hence is difficult to detect; however torsion’s fully-antisymmetric axial component \mathcal{A} is minimally coupled through covariant derivatives to fermion spins. Lämmerzahl[31] noted that results from Hughes-Drever experiments can place useful bounds on \mathcal{A} , and Kostelecký, Russell and Tasson[32] recently showed how experiments, such as the one we report here, determine all three spatial components of \mathcal{A} . Following Ref. [32], we find for minimal coupling (Ref. [32] considers more complex cases as well) that our results in Table VI constrain any background torsion field (assumed to be roughly constant over the region of the solar system) to

$$\begin{aligned}\mathcal{A}_X &= -4A_X/(3\hbar c) = (+4.5 \pm 8.9) \times 10^{-16} \text{ m}^{-1} \\ \mathcal{A}_Y &= -4A_Y/(3\hbar c) = (+1.2 \pm 8.9) \times 10^{-16} \text{ m}^{-1} \\ \mathcal{A}_Z &= -4A_Z/(3\hbar c) = (+2.7 \pm 29.8) \times 10^{-15} \text{ m}^{-1} .\end{aligned}\tag{50}$$

B. Boson-exchange constraints

1. *CP-violating monopole-dipole interactions*

The constraints on *CP*-violating monopole-dipole interactions extracted from our lab-fixed and solar and lunar-source data are shown in Fig. 14 (see also Table X). This new work improves over previous work[27–29] by factors of up to 10^4 .

2. *Velocity-dependent interactions*

The limits on velocity-dependent boson-exchange forces, extracted from our experimental bounds on interactions between the spin pendulum and the sun are given in Table X. Figure 15 shows range-dependence of the velocity-dependent couplings f_v and f_\perp . We are not aware of any previous measurements of such forces.

C. A test of the Equivalence Principle for spin?

It may be of some interest to interpret our constraints as an “equivalence-principle” test for intrinsic spin, i.e. to ask if the gravitational mass of an electron with its spin pointing

TABLE X: 1σ boson-exchange constraints from interactions with the Sun and Moon. Note that $f_v = 2g_A^e g_V^N$. The solar and lunar constraints assume $\lambda \gg 1.5 \times 10^{11}$ m and $\lambda \gg 4 \times 10^8$ m, respectively.

parameter	solar constraint	lunar constraint
$g_P^e g_S^N / (\hbar c)$	$(-3.5 \pm 8.5) \times 10^{-37}$	$(+0.2 \pm 1.6) \times 10^{-34}$
$f_\perp / (\hbar c)$	$(-0.1 \pm 2.1) \times 10^{-32}$	$(-1.1 \pm 8.6) \times 10^{-29}$
$g_A^e g_V^N / (\hbar c)$	$(+0.2 \pm 1.2) \times 10^{-56}$	$(-3.1 \pm 2.4) \times 10^{-50}$

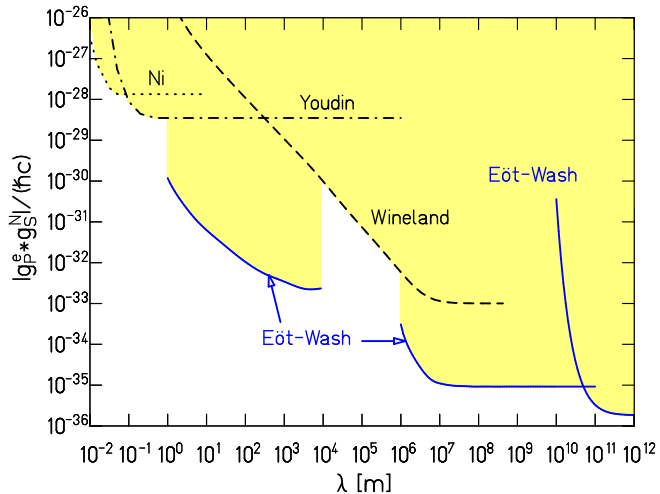


FIG. 14: (color online) Upper limits on $|g_P^e g_S^N| / (\hbar c)$ as a function of interaction range λ ; the shaded region is excluded at 95% confidence. Our results and previous work by Youdin et al.[27], Ni et al.[28] and Wineland et al.[29] are indicated by solid, dash-dotted, dotted and dashed lines, respectively. Our work does not provide constraints for $10 \text{ km} < \lambda < 10^3 \text{ km}$ because integration over the terrestrial surrounding is not reliable in this regime (see Ref. [20]).

toward the sun is identical to that of an electron whose spin points away from the sun. In this case the relevant parameter is

$$\tilde{\eta} \equiv \frac{[m_g]_t - [m_g]_a}{\frac{1}{2}([m_g]_t + [m_g]_a)} = \frac{2\beta_{\text{sun}}}{V_N}, \quad (51)$$

where the subscripts t and a refer to an electron whose spin points toward or away from the sun, β_{sun} is the component of our signal β that tracks the sun, and $V_N = -5.04 \times 10^{-3}$ eV is the Newtonian potential energy of a laboratory electron in the field of the sun. We find

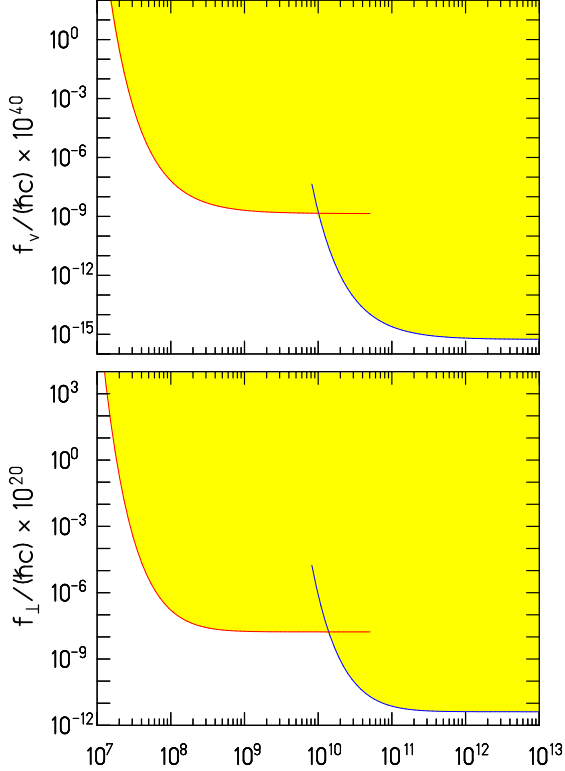


FIG. 15: (color online) Constraints on the velocity-dependent couplings f_v and f_{\perp} inferred from the infinite-range results in Table X. The shaded area is excluded at 95% confidence. In making this plot from the $\lambda = \infty$ results in Table X we neglected the eccentricities of the earth's and moon's orbits.

that $\beta_{\text{sun}} = (-0.62 \pm 1.30) \times 10^{-22}$ eV, which leads to

$$\tilde{\eta} = (+2.4 \pm 5.2) \times 10^{-20}, \quad (52)$$

where the errors are 1σ . A considerably tighter limit comes from considering electrons falling toward the center of our galaxy. In this case $V_N = m_e \Theta_0^2$ where $\Theta_0 = 220 \pm 20$ km/s is the velocity of the solar system around the center of the galaxy, which gives $V_N = -0.275 \pm 0.050$ eV. In this case we find $\beta_{\text{gal}} = (+0.27 \pm 1.50) \times 10^{-22}$ eV, which leads to

$$\tilde{\eta} = (+0.2 \pm 1.1) \times 10^{-21}. \quad (53)$$

D. Measurement of the spin density in SmCo₅

The absolute “gyrocompass” calibration of the spin content of our pendulum in Eq. 40 provides a clean comparison of the spin density, ρ_s , of room-temperature grade 22 SmCo₅ to that of Alnico 5,

$$\begin{aligned} \rho_s(\text{SmCo}_5) - \rho_s(\text{Alnico}) &= -N_p^{\text{exp}}/(V\eta) \\ &= (-3.66 \pm 0.08) \times 10^{22} \text{ spins/cm}^3, \end{aligned} \quad (54)$$

when the SmCo₅ and Alnico have identical magnetizations of $B_0 = 9.6 \pm 0.2$ kG. The quantities η and V are defined in Eq. 10. We have neglected the very small measured magnetic moment ($\mu_B = -0.04$) of Sm in SmCo₅ compared to the Co moment ($-8.97\mu_B$), so that the equality of the magnetic fields in the two materials implies that the magnetizations satisfied $M(\text{Co}) = M(\text{Alnico})$. The spin density in Alnico is

$$\begin{aligned} \rho_s(\text{Alnico}) &= B_0/(\mu_0\mu_B)f_{\text{Alnico}} \\ &= (7.85 \pm 0.17) \times 10^{22} \text{ spins/cm}^3, \end{aligned} \quad (55)$$

where f_{Alnico} is taken from Eq. A2. Therefore

$$\rho_s(\text{SmCo}_5) = (4.19 \pm 0.19) \times 10^{22} \text{ spins/cm}^3. \quad (56)$$

VIII. SUMMARY

We have shown that a torsion balance fitted with a spin pendulum can achieve a constraint of $\sim 10^{-22}$ eV on the energy required to flip an electron spin about an arbitrary direction fixed in inertial space. This is comparable to the electrostatic energy of two electrons separated by 90 AU. We then use this and related constraints to set sensitive limits on preferred-frame effects and non-commutative spacetime geometries. Our upper limits on the electron’s rotation-noninvariant parameters $|\mathbf{A}_{X,Y}^e| \leq 1.5 \times 10^{-22}$ eV and $|\mathbf{A}_Z^e| \leq 44 \times 10^{-22}$ eV are substantially smaller than previous work[22] and up to 5 orders of magnitude below the benchmark value $m_e^2/M_{\text{Planck}} = 2 \times 10^{-17}$ eV. Corresponding constraints on preferred-frame effects involving protons and neutrons are given in Refs. [23] and [25]. Interpreting our results as a constraint on non-commutative geometries we find that the minimum “observable” area is $|\Theta_{XZ}|$ or $|\Theta_{Y,Z}| \leq 4.9 \times 10^{-59} \text{ m}^2$, which corresponds to a length scale $\ell = 355 l_{\text{GUT}}$ where

$l_{\text{GUT}} = \hbar c / (10^{16} \text{ GeV})$. (Our limit $|\Theta_{XY}| \leq 1.5 \times 10^{57} \text{ m}^2$ is weaker because it is derived from a lab-fixed signal which has a larger scale factor uncertainty.) These limits assume that the electron remains point-like up to an energy scale of 1 TeV.

By analyzing 17 months of data, we obtained the first constraint on all 9 components of the Lorentz violating “boost” parameter \mathbf{C} for any particle. Our upper limits on the absolute values of these components ranges between 2×10^{-18} and 23×10^{-18} eV. To facilitate SME analyses, we also present constraints on \mathbf{C}' , the tensor helicity with respect to the sun. Our electron constraints have roughly the same sensitivity as related neutron constraints obtained with a dual-gas maser[25].

Our constraints on CP -violating monopole-dipole interactions, derived from laboratory-fixed and solar-source signals, improve on previous work by factors of up to 10^4 , while our results for interactions between the spin pendulum and the sun or moon provide the first sensitive test for exotic spin-and-velocity-dependent interactions of electrons.

Finally, our observation of the gyrocompass effect on the electron spins provides a precise result bearing on the electronic spin structure of Sm Co_5 . If we assume that effects from exotic physics are negligible, our measurements determine the density of polarized electrons in Sm Co_5 is $(4.19 \pm 0.19) \times 10^{-22} \text{ cm}^{-3}$ at a field of 9.6 kG.

We are now taking a new series of measurements that probe the interaction between two spins. This work is motivated by the recent development of a consistent model of gravity with spontaneous Lorentz-symmetry violation[5] that predicts dramatic new spin-spin forces. These new experiments also probe the velocity-independent spin-spin forces[11] that can arise from generic boson exchange.

Acknowledgments

Michael Harris and Stefan Baessler developed earlier versions of this apparatus. Their work provided us with essential experience that made this result possible. Jens Gundlach and CD Hoyle made useful comments about this experiment and Erik Swanson helped prepare some of the figures. We thank Nilendra Deshpande, Bogdan Dobrescu, David Kaplan, Alan Kostelecký and Jesse Thaler for inspiring conversations, and Tom Murphy, Jr for advice on the astronomical calculations. This work was supported by NSF Grants PHY0355012 and PHY0653863 and by DOE funding for the Center for Experimental Nuclear Physics and

TABLE XI: Magneto-mechanical factors of Fe-Co alloys from Ref. [34]. Percentages of Fe and Co are by weight.

% Fe	% Co	g'	f
75	25	1.918 ± 0.002	0.957
50	50	1.916 ± 0.002	0.956
25	75	1.902 ± 0.002	0.949

Astrophysics. CEC is grateful for an NSF Fellowship.

APPENDIX A: SPIN CONTRIBUTIONS TO THE MAGNETIZATION IN Sm Co_5 AND Alnico 5

1. Alnico 5

The composition of Alnico 5 by weight is 51% Fe, 24% Co, 14% Ni, 8% Al and 3% Cu and its magnetization arises primarily from the polarized spins of 3d electrons in the Fe and Co. The orbital moment of these electrons is small because of quenching in the inhomogeneous crystalline electric fields[33]. The polarized spins are confined to small, needle-shaped regions of Fe-Co alloy that precipitate out during heat treatment. Although we are not aware of direct measurements of the spin and orbital moments of Alnico 5, we can infer the spin fraction from “Einstein-De Haas” measurements[34] of the magneto-mechanical factors, g' , of magnetically “softer” Fe-Co alloys. The g' measurements determine, f , the fractional spin contribution to the magnetic moment via

$$f = \frac{2(g' - 1)}{g'} . \quad (\text{A1})$$

Table XI gives the measured spin fractions in various Fe-Co alloys. We adopt the mean and standard deviation of these values for the Alnico spin fraction,

$$f_{\text{Alnico}} = 0.953 \pm 0.005 \quad (\text{A2})$$

TABLE XII: Magnetic moments and spin fractions for RCo₅ compounds. Unless otherwise noted results are deduced from neutron scattering measurements[35, 36].

compound	$\mu(\text{Co}_I)$	$f(\text{Co}_I)$	$\mu(\text{Co}_{II})$	$f(\text{Co}_{II})$
Y Co ₅ ^a	-1.77(2) μ_B	0.74(5)	-1.72(2) μ_B	0.84(4)
Ce Co ₅ ^b		0.76		0.90
Sm Co ₅ ^c	-1.86(2) μ_B	0.72(6) ^d	-1.75(2) μ_B	0.85(6) ^d
Nd Co ₅ ^c	-1.95(3) μ_B	0.67(5)	-1.90(3) μ_B	0.80(3)

^aRef. [35, 36]

^bNMR measurement from Ref. [37]

^cRef. [36]

^dvalue inferred from neighboring compounds

2. Sm Co₅

a. Co in Sm Co₅

Although the magnetization of cobalt in Sm Co₅, as that of Alnico, arises primarily from polarized 3d electrons, the orbital moments are not as fully quenched because the rare earth atom alters the crystal lattice structure. Neutron[15, 35, 36] and photon[17] scattering studies, as well as NMR experiments[37], have shown that the Co atoms in R Co₅ (R is one of the rare earth elements) occupy two different crystal sites; 2 atoms in the 2c site (Co_I) and 3 in the 3g site (Co_{II}). Although the spin fraction of the Co magnetization in Sm Co₅ has not been measured, experiments consistently find that the Co magnetic moments in R Co₅ compounds are independent of temperature and, as shown in Table XII, vary only slightly across the rare earth series. We assume that the Co spin fractions also vary only slightly with R to infer $f(\text{Co}_I)$ and $f(\text{Co}_{II})$ for Sm Co₅ as given in Table XII. The total spin moment of the 5 Co atoms

$$\begin{aligned}
 \mu_S(\text{Co}) &= 2f(\text{Co}_I) \mu(\text{Co}_I) + 3f(\text{Co}_{II}) \mu(\text{Co}_{II}) \\
 &= (-7.14 \pm 0.39) \mu_B , \\
 \mu(\text{Co}) &= 2\mu(\text{Co}_I) + 3\mu(\text{Co}_{II})
 \end{aligned}$$

$$= (-8.97 \pm 0.10) \mu_B , \quad (\text{A3})$$

which implies that

$$f_{\text{Co}} = \mu_S(\text{Co})/\mu(\text{Co}) = 0.80 \pm 0.04 . \quad (\text{A4})$$

b. Sm in Sm Co₅

The Sm atoms in Sm Co₅ are in the 3⁺ ionic state with a (4*f*)⁵(6*s*)² electronic configuration. Hund's rules predict that the free Sm³⁺ ion's orbital momentum has the largest possible antisymmetric value of $L = 5$ and that the spins are in the symmetric $S = 5/2$ state. Therefore one expects large orbital as well as spin contributions to the magnetic moment. One also expects that the ion's ground state has S and L coupled to the minimum $J = 5/2$. This simple model predicts $\mu = -0.714 \mu_B$, $\mu_S = +3.57 \mu_B$ and $\mu_L = -4.29 \mu_B$. However, the Sm ions are embedded in a lattice and the crystalline and exchange fields alter this simple picture. Neutron scattering experiments[15] on Sm Co₅ find that $\mu(\text{Sm}) = -0.38 \mu_B$ at a temperature of 4.2K. However, at room temperature, $k_B T$ becomes comparable to the splitting of the magnetic substates and thermal population of the various M_J states causes the measured Sm magnetic moment to be very small, $\mu(\text{Sm}) = -0.04 \mu_B$ [15]. Using the Sm wavefunctions in Ref. [15], we calculate that at the temperature maintained during our experiments

$$\mu_S(\text{Sm}) = +3.56 \mu_B \quad (\text{A5})$$

The X-ray magnetic Compton scattering measurement reported in Ref. [17] probes the spin moment of Sm in Sm Co₅ directly, but provides no information about the total magnetic moment. The ratio of Co to Sm spin moments from this measurement, $R = -0.23 \pm 0.04$, together with Eq. A3, corresponds to

$$\mu_S(\text{Sm}) = +1.67 \pm 0.31 \mu_B . \quad (\text{A6})$$

c. Ratio of Sm to Co spin moments

Our calculation of the number of polarized electrons in our pendulum, Eq. 13, depends on R , the ratio of Sm to Co spin moments. The neutron scattering results in Eqs. A5 and A3 give

$$R \equiv \mu_S(\text{Sm})/\mu_S(\text{Co}) = -0.50 . \quad (\text{A7})$$

On the other hand the photon scattering work[17] directly gives

$$R = -0.23 \pm 0.04 . \tag{A8}$$

We accomodate this difference by assuming that R is equally likely to lie anywhere between these two values.

APPENDIX B: “FEETBACK” TILT ELIMINATION SYSTEM

We developed a digital feedback system that continuously corrects for the varying tilt of the laboratory floor and imperfections in the turntable itself. It analyses inputs from an orthogonal pair of co-rotating electronic tilt sensors and, every 2 complete revolutions of the turntable, computes the tilt as a function of turntable angle and cancels this predicted tilt by controlling the length of feet that support the turntable. The performance of the leveling system is shown in Fig. 16 which demonstrates that the system compensates not only for the slowly-varying tilt of the laboratory floor but also for the more rapid variations caused by imperfections in the turntable bearing.

The tilt is measured by Applied Geomechanics Inc. inclinometers (AGI’s) mounted on the rotating apparatus close to the upper attachment point of the pendulum’s suspension fiber. A constant tilt of the rotation axis appears as a 1ω signal on each AGI, with a 90° phase difference between the two units. The analog signals of the AGI’s are digitized by the data acquisition system and analyzed to determine the tilt with a precision of $\approx 1 \mu\text{rad}/\sqrt{\text{Hz}}$. This tilt is then removed by adjusting the lengths of 2 of the 3 feet upon which the apparatus rests. The lengths of the two feet are controlled by varying their temperatures. Figure 17 shows a cross section through one foot. The expanding and shrinking components of a foot consist of two lead rings (1) which are soldered to a copper disk (2). Thermal energy can be pumped into or out of the copper disk by a Peltier element (3) thermally coupled to a brass block (4) that is held at constant temperature by circulating water from a temperature-stabilized reservoir. Two G10 rings (5) thermally isolate the lead rings from the laboratory floor and from a stainless steel disk on top, upon which the apparatus rests. The Peltier element and the brass block are clamped to the copper disk by one bolt (6). Specially formed G10 pieces provide thermal isolation between the bolt, the copper disk and the brass block.

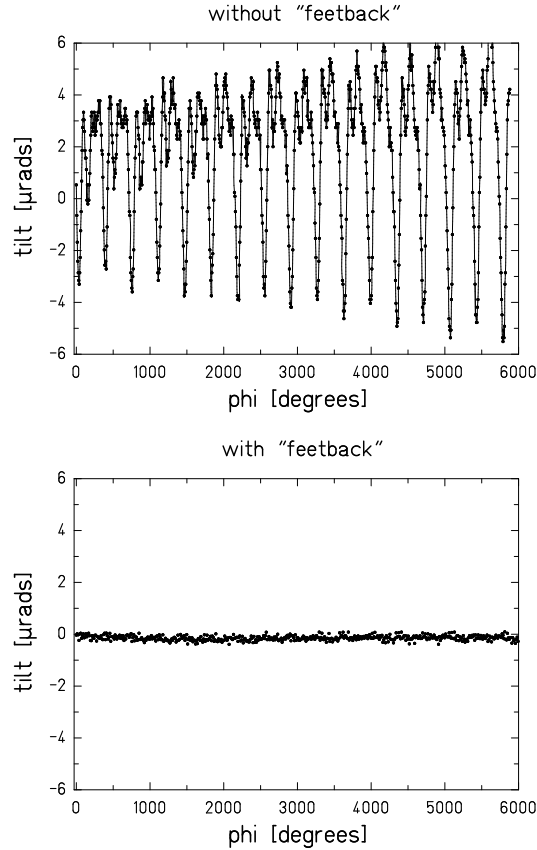


FIG. 16: Performance of the “feedback system” showing the tilt measured by co-rotating level sensors. Upper panel: “feedback” off. The rapid fluctuations arise from imperfections in the turntable bearing, slower variations arise from the varying tilt of the laboratory floor. Lower panel: “feedback” on.

The thermal capacity and thermal resistance of the copper disk and the lead rings produce a 14-second delay in the expansion of the lead rings compared to the change in the heat flux provided by the Peltier element. In addition, the thermal conductivity of the Peltier element, which connects the copper disk to the temperature reservoir, affects the time constant of the response. Taking these factors into account, we developed a model, shown in Fig. 18, to predict a foot’s response to a change in heat flux delivered by its Peltier element. The model poses no problem for a real-time calculation because it can be solved analytically. The delayed response of the feet together with an 8-second integration time of the AGI’s leads to a low-pass behavior of the leveling system. Therefore the response of the feet to fast changes of the tilt caused by imperfections of the ball bearings in the turntable is limited.

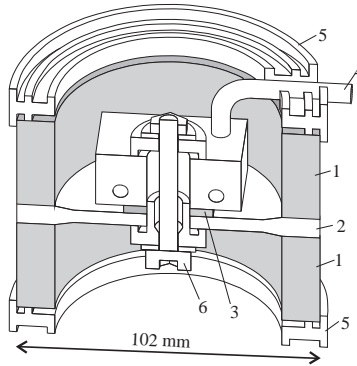


FIG. 17: Cross section of a foot of the Eöt-Wash rotating torsion balance.

The tilt caused by the imperfections of the bearing is periodic in the turntable angle. This allowed us to express the bearing tilt in Fourier coefficients of the turntable angle. Once these Fourier coefficients are calculated, they are fed forward to compensate for the bearing imperfections. A simplified flow chart of the feedback loop is shown in Fig. 18. With the feedback switched on, a typical tilt of a few μrad per day is reduced to less than 10 nrad.

After the simple model described above was implemented, we found it necessary to add one further refinement. The DC offsets of the AGI's drift slowly in time. A feedback system that holds constant the AGI signals does not guarantee true level. With the feedback on, a drifting offset produces a 1ω AGI signal with the opposite phase lag between the two sensors compared to a true tilt. Our model extracts this Fourier component and uses it to determine the AGI readings that correspond to true level.

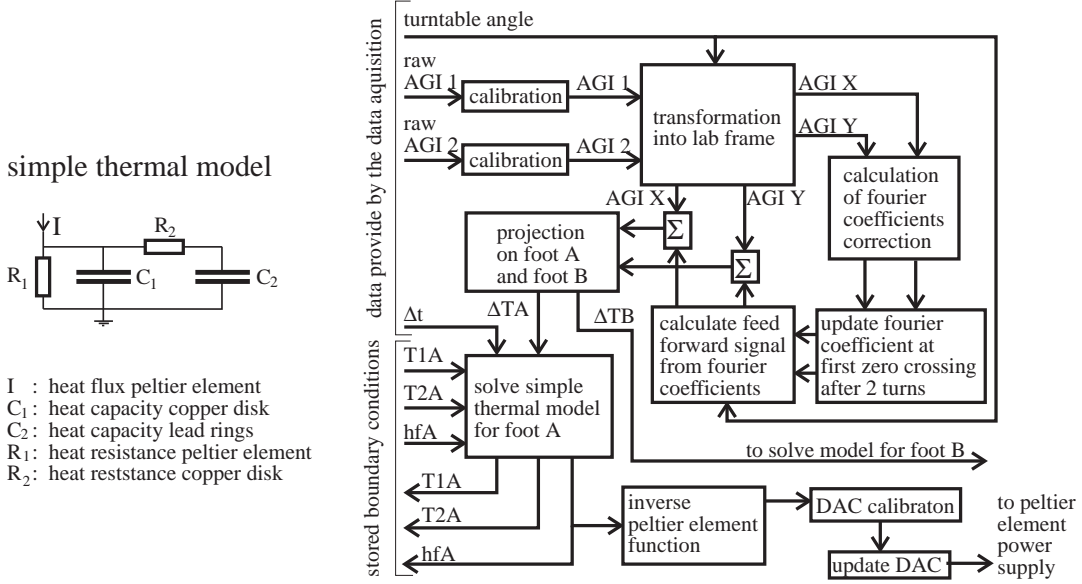


FIG. 18: Thermal model and flow chart of the simplified feedback loop implemented at the Eöt-Wash II rotating torsion balance

-
- [1] B.R. Heckel *et al.*, Phys. Rev. Lett. **97**, 021603 (2006).
 - [2] D. Colladay and V. A. Kostelecký, Phys. Rev. D **55**, 6760 (1997); Phys. Rev. D **58**, 116002 (1998); V. A. Kostelecký, Phys. Rev. D **69**, 105009 (2004).
 - [3] V. A. Kostelecký and N. Russell, arXiv:0801.0287 (2008).
 - [4] R. Bluhm and V. A. Kostelecký, Phys. Rev. Lett. **84**, 1381 (2000).
 - [5] N. Arkani-Hamed *et al.*, J. High Energy Phys. **0405**, 074 (2004).
 - [6] N. Arkani-Hamed H-C. Cheng, M. Luty, and J. Thaler, J. High Energy Phys. **07**, 029 (2005).
 - [7] S.M. Carroll, J.A. Harvey, V.A. Kostelecký, C.D. Lane and T. Okamoto, Phys. Rev. Lett. **87**, 141601 (2001).
 - [8] I. Hinchliffe, N. Kersting and Y.L. Ma, Int. J. Mod. Phys. **A19**, 179 (2004); hep-ph/0205040.
 - [9] A. Anisimov, T. Banks, M. Dine and M. Graesser, Phys. Rev. D **65**, 085032 (2002); hep-ph/0106356.
 - [10] J. E. Moody and F. Wilczek, Phys. Rev. D **30**, 130 (1984).
 - [11] B. A. Dobrescu and I. Mocioiu, J. High Energy Phys. **0611**, 5 (2006); hep-ph/0605342.
 - [12] S. Baeßler *et al.*, Phys. Rev. Lett. **83**, 3585 (1999).

- [13] Y. Su *et al.*, Phys. Rev. D **50**, 3614 (1994).
- [14] C. D. Hoyle *et al.*, Phys. Rev. D **70**, 042004 (2004).
- [15] D. Givord, J. Laforest, J. Schweizer and F. Tasset, J. Appl. Phys. **50**, 2008 (1979).
- [16] P. Tils, M. Loewenhaupt, K. H. J. Buschow and R. S. Eccleston, J. Alloys and Compounds **289**, 28 (1999).
- [17] A. Koizumi, N. Sakai, N. Shirai and M. Ando, J. Phys. Soc. Japan **66**, 318 (1997).
- [18] Magnet Sales and Manufacturing, Inc. (www.magnetsales.com).
- [19] J. Meeus, *Astronomical Algorithms, 2nd Edition*, Willman-Bell, Richmond VA (1998).
- [20] E. G. Adelberger *et al.*, Phys. Rev. D **42**, 3267 (1990).
- [21] M. M. Nieto, T. Goldman and R.J. Hughes, Phys. Rev. D **36**, 3688 (1987).
- [22] L. S. Hou, W. T. Ni, and Yu-Chum. Li, Phys. Rev. Lett. **90**, 201101-1 (2003).
- [23] D. F. Phillips *et al.*, Phys. Rev. D **63**, 111101(R) (2001).
- [24] M. A. Humphrey *et al.*, Phys. Rev. A **68**, 063807 (2003).
- [25] F. Canè *et al.*, Phys. Rev. Lett. **93**, 230801 (2004).
- [26] V. A. Kostelecký, private communication (2007).
- [27] A. N. Youdin, D. Krause, K. Jagannathan, L. R. Hunter and S. K. Lamoreaux, Phys. Rev. Lett. **77**, 2170 (1996).
- [28] W. T. Ni, S. S. Pan, H. C. Yeh, L. S. Hou and J. Wan, , Phys. Rev. Lett. **82**, 2439 (1999).
- [29] D. J. Wineland, J. J. Bollinger, D. J. Heinzen, W. M. Itano, M. G. Raizen, Phys. Rev. Lett. **67**, 1735 (1991).
- [30] I.L. Shapiro, Phys. Rep., **357**, 113 (2002).
- [31] C. Lämmerzahl, Phys. Lett. A **228**, 233 (1997).
- [32] V.A. Kostelecký, N. Russell and J.D. Tasson, Phys. Rev. Lett. **100**, 111102 (2008).
- [33] R. M. Bozorth, *Ferromagnetism*, Van Nostrand, New York, NY (1951).
- [34] G. G. Scott and H. W. Sturmer, Phys. Rev. **184**, 490 (1969).
- [35] J. Schweizer and F. Tasset, J. Phys. F, **10**, 2799 (1980).
- [36] D. Givord, J. Laforest, R. Lemaire and Q. Lu, J. Mag. and Mag. Mat. **31-34**, 191 (1983).
- [37] H. Yoshie *et al.*, J. Phys. Soc. Japan **57**, 2525 (1988).
- [38] H. Müller *et al.*, Phys. Rev. Lett. **99**, 050401 (2007).